

Magnetic Fields in Massive Star-Forming Regions (MagMaR) II. Tomography Through Dust and Molecular Line Polarization in NGC 6334I(N)

PAULO C. CORTÉS,^{1,2} PATRICIO SANHUEZA,^{3,4} MARTIN HOUDE,⁵ SERGIO MARTÍN,^{6,1} CHARLES L. H. HULL,^{7,1,8}
JOSEP M. GIRART,^{9,10} QIZHOU ZHANG,¹¹ MANUEL FERNANDEZ-LOPEZ,¹² LUIS A. ZAPATA,¹³ IAN W. STEPHENS,¹⁴
HUA-BAI LI,¹⁵ BENJAMIN WU,¹⁶ FERNANDO OLGUIN,¹⁷ XING LU,¹⁸ ANDRES E. GUZMÁN,¹⁸ AND FUMITAKA NAKAMURA^{18,4}

¹Joint ALMA Observatory, Alonso de Córdova 3107, Vitacura, Santiago, Chile

²National Radio Astronomy Observatory, 520 Edgemont Road, Charlottesville, VA 22903, USA

³National Astronomical Observatory of Japan, 2-21-1 Osawa, Mitaka, Tokyo 181-8588, Japan

⁴Department of Astronomical Science, SOKENDAI (The Graduate University for Advanced Studies), 2-21-1 Osawa, Mitaka, Tokyo 181-8588, Japan

⁵Department of Physics and Astronomy, The University of Western Ontario, London, ON N6A 3K7, Canada

⁶European Southern Observatory, Alonso de Córdova 3107, Vitacura, Santiago, Chile

⁷National Astronomical Observatory of Japan, Alonso de Córdova 3788, Office 61B, 7630422, Vitacura, Santiago, Chile

⁸NAOJ Fellow

⁹Institut de Ciències de l'Espai (ICE-CSIC), Campus UAB, Carrer de Can Magrans S/N, E-08193 Cerdanyola del Vallés, Catalonia

¹⁰Institut d'Estudis Espacials de Catalunya (IEEC), E-08034 Barcelona, Catalonia

¹¹Harvard-Smithsonian Center for Astrophysics, 60 Garden Street, Cambridge, MA 02138, USA

¹²Instituto Argentino de Radioastronomía (CCT-La Plata, CONICET; CICPBA), C.C. No. 5, 1894, Villa Elisa, Buenos Aires, Argentina

¹³Instituto de Radioastronomía y Astrofísica, Universidad Nacional Autónoma de México, P.O. Box 3-72, 58090, Morelia, Michoacán, México

¹⁴Department of Earth, Environment and Physics, Worcester State University, Worcester, MA 01602, USA

¹⁵Department of Physics, The Chinese University of Hong Kong, Shatin, NT, Hong Kong SAR, People's Republic of China

¹⁶NVIDIA Research, 2788 San Tomas Expressway, Santa Clara, CA 95051

¹⁷Institute of Astronomy and Department of Physics, National Tsing Hua University, Hsinchu 30013, Taiwan

¹⁸National Astronomical Observatory of Japan, National Institutes of Natural Sciences, 2-21-1 Osawa, Mitaka, Tokyo 181-8588, Japan

ABSTRACT

Here, we report ALMA detections of polarized emission from dust, CS($J = 5 \rightarrow 4$), and C³³S($J = 5 \rightarrow 4$) toward the high-mass star-forming region NGC6334I(N). A clear “hourglass” magnetic field morphology was inferred from the polarized dust emission which is also directly seen from the polarized CS emission across velocity, where the polarization appears to be parallel to the field. By considering previous findings, the field retains a pinched shape which can be traced to clump length-scales from the envelope scales traced by ALMA, suggesting that the field is dynamically important across multiple length-scales in this region. The CS total intensity emission is found to be optically thick ($\tau_{\text{CS}} = 32 \pm 12$) while the C³³S emission appears to be optically thin ($\tau_{\text{C}^{33}\text{S}} = 0.1 \pm 0.01$). This suggests that sources of anisotropy other than large velocity gradients, i.e. anisotropies in the radiation field are required to explain the polarized emission from CS seen by ALMA. By using four variants of the Davis-Chandrasekhar-Fermi technique and the angle dispersion function methods (ADF), we obtain an average of estimates for the magnetic field strength onto the plane of the sky of $\langle B_{\text{pos}} \rangle = 16$ mG from the dust and $\langle B_{\text{pos}} \rangle \sim 2$ mG from the CS emission, where each emission traces different molecular hydrogen number densities. This effectively enables a tomographic view of the magnetic field within a single ALMA observation.

Keywords: Unified Astronomy Thesaurus concepts: Polarimetry (1278); Dust continuum emission (412); Star formation (1569); Protostars (1302); Interstellar dust (836); Young stellar objects (1834); Interstellar magnetic fields (845)

1. INTRODUCTION

Since the early days of millimeter astronomy, we have made significant progress in our understanding of the physical mechanisms behind star formation in molecular clouds. Because molecular clouds in the interstellar medium are composed of partially ionized gas and dust, magnetic fields are unavoidable; however, their role in formation of stars remains not well understood. Although the past 25 years have produced significant advancement in the understanding of the role of magnetic fields in the star-formation process (see review by Hull & Zhang 2019), it is just now that new observational facilities are giving us the required resolution, sensitivity, and mapping capabilities that are finally allowing us to study the magnetic field in significant greater detail.

Perhaps where the role of magnetic field is least understood is in high mass star forming regions (HMSFR). The main two theorized formation pathways for high mass stars, or stars with masses $\geq 8 M_{\odot}$, are either that there is a monolithic collapse from an initial massive dense core, which is regulated by non-thermal motions or turbulence (McKee & Tan 2003; Krumholz et al. 2007), or that stars form from aggregates of smaller clumps (each with an initial mass of approximately the thermal Jeans mass) that compete for gas and dust accretion and may merge to produce larger proto-stellar cores (Bonnell et al. 2004, 2007). Because the magnetic field has been shown to be ubiquitous in the ISM, the dynamical evolution of the gas and dust in high mass star-forming regions will be inevitably influenced by magnetic fields.

NGC6334 is a Giant Molecular Cloud (GMC) in the southern hemisphere. This GMC is located inside the Sagittarius-Carina spiral arm at a distance of about 1.3 ± 0.3 kpc (Chibueze et al. 2014) and has an estimated line mass of $\sim 1000 M_{\odot} \text{ pc}^{-1}$ with an extension of ~ 10 pc (André et al. 2016). The brightest regions studied in the millimeter and sub-millimeter are NGC6334I and NGC6334I(N) (McCutcheon et al. 2000; Hunter et al. 2014, 2017; Sadaghiani et al. 2020), where both regions appear to harbor high mass star formation. Besides the large scale mapping of polarized dust emission done by Planck (Planck Collaboration XXXV et al. 2016), the magnetic field in NGC6334I(N) has been mapped via polarized dust emission at angular resolutions from $\sim 4''$ (Li et al. 2006), $\sim 20''$ Vaillancourt (2011), $\sim 14''$ (Arzoumanian et al. 2021), and $\sim 2''$ (Zhang et al. 2014;

Li et al. 2015) which found a field shape evolving from a clear pinch at the high density peaks at large scales to an “hourglass” shape at shorter scales. We follow the nomenclature used by Hull & Zhang (2019), where we refer to cloud scales to structures ~ 10 pc, clump scales ~ 1 pc, core scales between 0.1 to 0.01 pc, and envelope scales to structures ~ 1000 au. In this paper, we present ALMA results of spectro-polarimetry and dust continuum polarimetry towards NGC6334I(N). This target was observed as part of the Magnetic fields in Massive star-forming Regions (MagMaR) survey that in total contains 30 sources. Details on the survey and source selection will be given in Sanhueza et al. (2021, in prep.). Early results on specific targets are presented in Fernández-López et al. (2021); G5.89–0.39) and Sanhueza et al. (2021); IRAS 18089-1732. The paper is organized as follows, Section 2 presents the observation setup including calibration and data reduction analysis, Section 3 shows the results from polarized dust and CS emission, Section 4 aggregates the analysis about the origin and ambiguities of the CS polarized emission, the magnetic field morphology and the strength estimation along with comparison to other high mass star forming regions. Finally, Section 5 presents the summary and conclusion from this work.

2. OBSERVATIONS

The NGC6334I(N) source is part of project 2018.1.00105.S, which was executed twice in session mode (see chapter 8 in Cortes et al. 2021, for details about the session observing mode), during December 2018 and May 2019 under configuration C43-4 (providing baseline lengths from 15 to 783 m). The correlator was configured to yield full polarization cross correlations using Frequency Division Mode (or FDM giving XX, XY, YX, and YY), and includes spectral windows to map the dust continuum and windows centered on major molecular line rotational transitions. The band-pass was calibrated using J1427-4206 for session 1 and J1924-2914 for session 2. The time dependant gain and the polarization instrumental terms were calibrated using J1717-3342 and J1751+0939, respectively. For calibration we used CASA version 5.4 and version 5.6 for imaging (McMullin et al. 2007). To image the continuum we manually extracted the line-free channels from each spectral window, which we later phase-only self-calibrated using a final solution interval of 60 seconds.

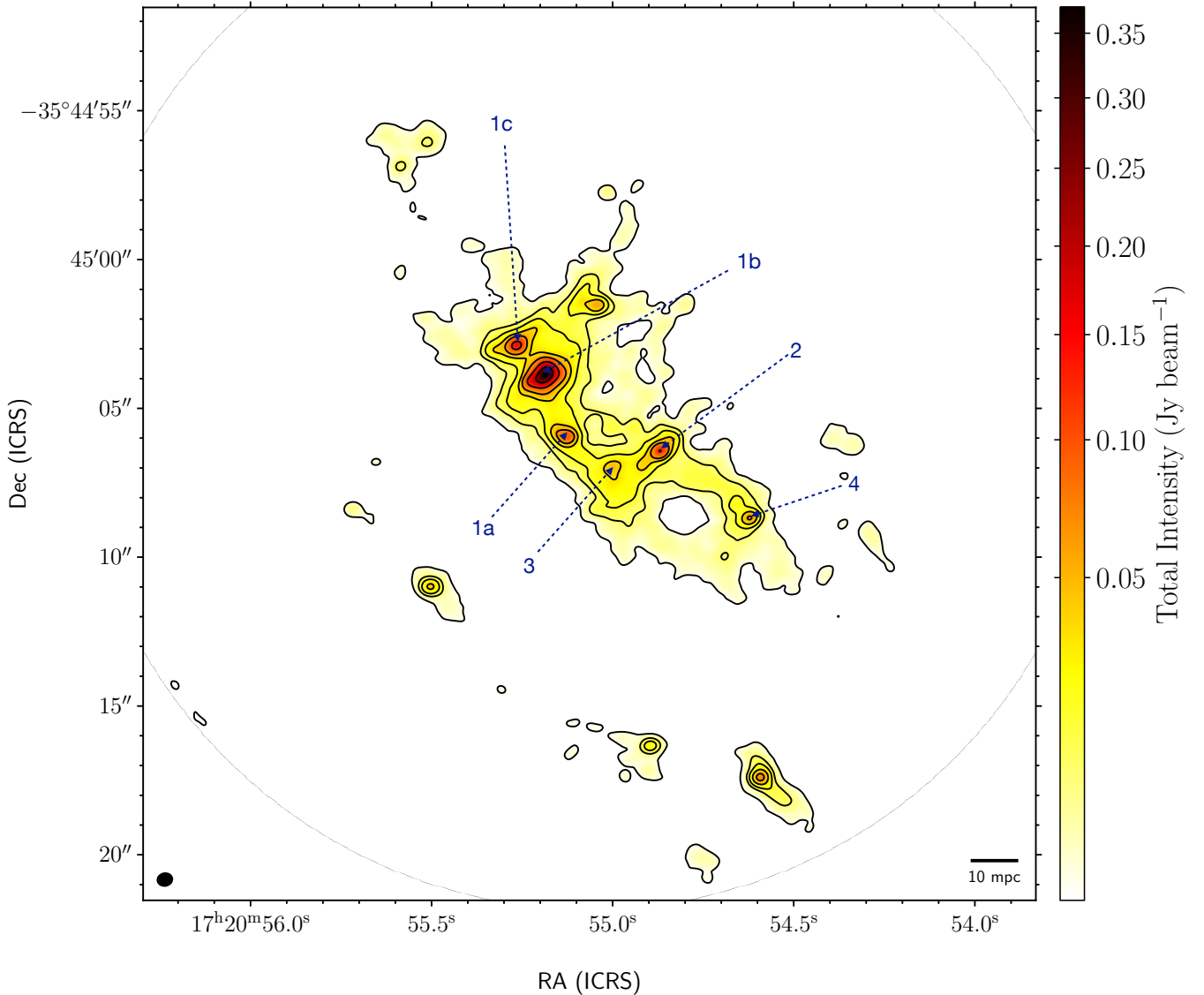


Figure 1. The Figure shows the total intensity dust emission at 1 mm from NGC6334I(N). The color scale is in mJy beam^{-1} , as indicated by the color bar. The contours correspond to the total intensity and are plotted at levels of 1.7, 8.8, 17.7, 35.3, 58.9, 117.8, 235.6, and 353.4 mJy beam^{-1} with an rms for the primary beam corrected map of $\sigma = 1.1 \text{ mJy beam}^{-1}$, where the beam is shown in the bottom-left corner as a solid, black ellipse. The main sources as reported by Hunter et al. (2014) are indicated by the segmented arrows.

These solutions were then applied to the CS and C^{33}S spectral windows before imaging the lines, which were binned to 2 km s^{-1} per channel. The statistics of the flat Stokes images, before debiasing, for both continuum and channel maps are shown in Table 1. All of the Stokes parameters were imaged independently using the CASA task *tclean*, which yielded an angular resolution of approximately $0.5'' \times 0.3''$, with a position angle of -78° . The data were primary beam corrected and debiased

pixel-by-pixel following Wardle & Kronberg (1974); Hull & Plambeck (2015). Finally, we analyzed the data in the scope of the normalization issue discovered in ALMA data¹. A brief description can be found in appendix B.

¹ See the ALMA knowledge base article at <https://help.almascience.org/kb/articles/what-errors-could-originate-from-the-correlator-spectral-normalization-and-tsys-calibration>

3. RESULTS

3.1. Polarized Dust Continuum Emission

Figure 1 shows the total intensity (Stokes I) thermal dust continuum emission map from NGC6334I(N) along with the main sources identified by Hunter et al. (2014) from their Sub Millimeter Array (SMA) data. The total intensity dust emission map shows an elongated filament with two cores (1b and 1c) dominating the emission and, what appears to be, a cavity in the dust emission towards the southern part of the filament. In this work we focus on the magnetic field leaving the cores mass and density statistical analysis for further work (Cortés et al. in prep.). Figure 2, shows the magnetic field morphology onto the plane of the sky as derived from polarized dust emission. The magnetic field morphology is derived by assuming grain alignment by magnetic fields, where the polarization position angles are rotated by 90° to obtain the field direction. The field pattern covers most of the NGC6334I(N) filament showing a clear indication of an “hourglass” shape over the 1b and 1c cores (inside the purple oval in Figure 2). Additionally, to the south of the main two cores we see that the field is also pinched over the third brightest core in the region (1a), with the field smoothly connecting to the aforementioned “hourglass” component. A pinched field morphology in NGC6334I(N) has been suggested from cloud to core scales by Li et al. (2015). In fact, Li et al. traced an “hourglass” morphology with the SMA at core scales, which we reproduced here in Figure 3 by using data from Zhang et al. (2014). In this work we are further tracing the magnetic field morphology with ALMA from core to envelope scales. Note, we are referring to a pinched morphology instead of “hourglass” for the whole set of scales; we will discuss this in section 4.2.

Recently, observations with the James Clerk Maxwell Telescope (JCMT) of polarized dust emission at $850 \mu\text{m}$ revealed a detailed field morphology of NGC6334I(N) at clump scales ($14''$ resolution, Arzoumanian et al. 2021). To compare with ours, we show a zoomed map of the JCMT data (see Figure 3, left panel), where the pinched morphology is seen over a broader region encompassing both NGC6334I(N) and NGC6334I sources (NGC6334I is not covered by the ALMA data presented here) and outlined by translucent red lines. Over the NGC6334I(N) filament, the JCMT data shows a mostly uniform pattern covering the region mapped by ALMA (see yellow circle in Figure 3). Furthermore, Arzoumanian et al. compared the JCMT data to Planck data, where pinching of the field is only seen at the North-East edge of the cloud at the scales traced by Planck.

Although these new data show a slightly different scenario as the one proposed by Li et al. (2015), the magnetic field appears to evolve coherently from clump to core-envelope scales (see section 4.2 for a discussion).

To the SW of the filament, a cavity is seen in the dust emission traced by ALMA (see Figure 2). This cavity is well encircled by the field, which covers most of its perimeter. Magnetic fields along cavity walls produced by outflows have been seen in a number of low-mass star-forming regions (Hull et al. 2017; Maury et al. 2018; Le Gouellec et al. 2019; Hull et al. 2019). Coincidentally, the blue lobe of the CS outflow, previously discovered by McCutcheon et al. (2000) and also reported here, appears to be co-spatial with the cavity.

To ascertain the importance of the magnetic field in NGC6334I(N), we estimate its strength onto the plane of the sky component, B_{pos} , using a number of variants of the Davis, Chandrasekhar, and Fermi method (or DCF: Davis 1951; Chandrasekhar & Fermi 1953; Heitsch et al. 2001; Falceta-Gonçalves et al. 2008), by using the angle dispersion function method (or ADF: Hildebrand et al. 2009; Houde et al. 2009, 2013a, 2016), and by using a recently derived approach for DCF which considers magnetosonic perturbations instead of Alfvén waves (Skalidis & Tassis 2021). We will discuss the applicability of such methods to regions such as NGC6334I(N) in section 4.3. The computations were executed by following Cortés et al. (2019) for the DCF² variants and following Houde et al. (2009, 2016) for the dispersion function analysis. We obtained field-strength estimates by considering only the emission within the purple ellipse shown in Figure 2 (see Table 3 for the results). This is justified because is within this region that we have obtained sufficient overlap between the polarized dust and CS emission tracing the hourglass shape of the magnetic field (see section 3.2). The B_{pos} estimates range between 1.4 and 23.6 mG, with an average of $\langle B_{\text{pos}} \rangle = 16$ mG. In contrast with previous works, here we estimate the field strength in a self-consistent manner by using parameter values derived directly from our data. For instance, we derive the velocity dispersion from our C^{33}S spectrum, which by being optically thin (see Section 3.2), it traces the turbulent motions inside the region. The column and volume densities are also derived directly from the Stokes I dust and CS emissions; we compute all values within the same region used to derive the polarization position angle dispersion ($\delta\phi$). To derive column density

² The modifications to DCF proposed by Skalidis & Tassis (2021) require to change $\delta\phi$ by $\sqrt{\delta\phi}$ and a change of $1/\sqrt{2}$ scaling factor and thus the practicalities of the computation are the same as with the regular DCF variants

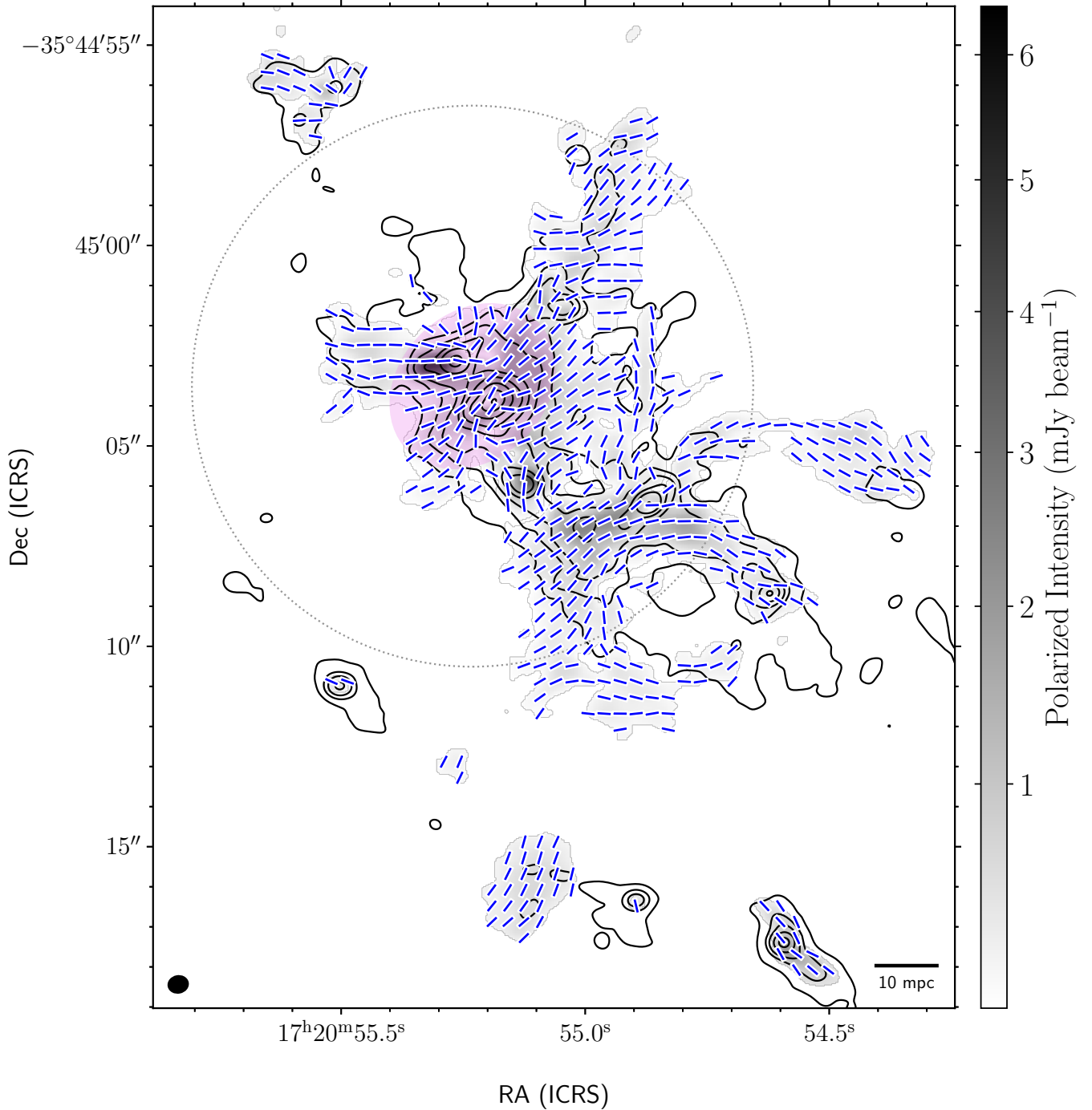


Figure 2. The magnetic field morphology onto the plane of the sky in NGC6334I(N), as derived from the 1.3 mm polarized dust emission is shown here. The blue line segments correspond to emission over $3\sigma = 50 \mu\text{Jy}$ in polarized intensity after debiasing. The line segments are normalized and plotted once per synthesized beam (coarser than Nyquist sampling by a factor of two in each dimension), where the beam size is $0''.5 \times 0''.3$; the beam is shown in the bottom-left corner as a solid, black ellipse. Gray scale shows the polarized intensity in mJy beam^{-1} , as indicated by the color bar, and is plotted starting from $600 \mu\text{Jy beam}^{-1}$. The contours correspond to the total intensity and are plotted at levels of 1.7, 8.8, 17.7, 35.3, 58.9, 117.8, 235.6, 353.4, and $471.2 \text{ mJy beam}^{-1}$ with an rms for the primary beam corrected map of $\sigma = 1.1 \text{ mJy beam}^{-1}$. The purple oval encloses the 1b and 1c cores identified by Hunter et al. (2014) also corresponding to the region used to estimate the magnetic field strength from the plane of the sky. The dotted circle represents the field of view of a single JCMT pointing in the data presented by Arzoumanian et al. (2021).

from dust emission, we followed the standard approach (Hildebrand 1983) assuming a dust opacity of $\kappa_{1.3\text{mm}} = 0.01 \text{ cm}^2 \text{ g}^{-1}$ (Ossenkopf & Henning 1994), which assumes a gas to dust mass ratio of 100:1, and an average dust temperature of $T_{\text{dust}} = 50 \text{ K}$ (Sadaghiani et al. 2020). We estimate the volume density by assuming a cylindrical ellipsoid as the geometrical shape of the purple ellipse in Figure 2, where the height of the cylinder is taken as the mean of the major and minor axes of the ellipse, which equals $3''.6$, or 22 mpc at the distance of NGC6334I(N). We also use a mean molecular weight of $\mu = 2.8$ which assumes that the gas has a 70% H_2 content and it is not stratified (Kirk et al. 2013). As a result, the uncertainties in the magnetic field strength estimation result primarily from the assumptions behind the validity of the DCF method and the geometrical assumption used to compute the density. The dispersion angle analysis is discussed in Section 4.3.

3.2. The polarized emission from CS ($J = 5 \rightarrow 4$) and C^{33}S ($J = 5 \rightarrow 4$)

We detect CS ($J = 5 \rightarrow 4$) emission, in total intensity, along the NGC6334I(N) filament across a velocity range from -40 to 20 km s^{-1} . Here, we focus primarily on the polarization properties of the emission and leave a detailed analysis of the gas kinematics to a future work (Cortés et al. in prep). We analyze the CS ($J = 5 \rightarrow 4$) and C^{33}S ($J = 5 \rightarrow 4$) spectra from the same region used to estimate the magnetic field strength from polarized dust emission (see Figure 4 for the spectra). Because C^{33}S is an isotopologue of the CS molecule, we can assume that both species are co-spatially located and thus we can use the C^{33}S emission, likely optically thin, to estimate the properties of the CS gas. To estimate the column density and optical depth of the lines, we used the MADCUBA software package to model the CS and C^{33}S line profiles (Martín et al. 2019); the model is shown in Figure 4, right panel. Under local thermodynamic equilibrium (LTE) conditions, the three spectral features of the classic asymmetric top methyl formate (CH_3OCHO) detected close to the C^{33}S line (see Figure 4) allow us to put a good constraint to the excitation temperature, which was found to be $T_{\text{ex}} = 220 \pm 80 \text{ K}$. Note, this temperature is likely probing a gas kinetic temperature, which is significantly higher than the assumed dust temperature, where the CS emission probably arises from a cooler layer than CH_3OCHO . Although this temperature seem high, it is not uncommon to find such excitation temperatures when a hot molecular core (HMC) has developed, which is the case in NGC6334I(N) 1b (Hunter et al. 2014). There, complex organic molecules such as methyl formate act as excellent thermometers

for the gas temperature. For instance, in W43-Main MM1 Sridharan et al. (2014) found an excitation temperature close to 400 K when considering spectral features of methyl cyanide in their data. Assuming that the C^{33}S emission is thermalized to this temperature and a source size of $1''$ as derived from the fit to the integrated emission, we obtain a C^{33}S total column density $N_{\text{C}^{33}\text{S}} = 1.0 \pm 0.1 \times 10^{15} \text{ cm}^{-2}$, with a peak optical depth of $\tau_{\text{C}^{33}\text{S}} = 0.18 \pm 0.02$. Scaling the C^{33}S emission using the sulphur 32/33 relative abundance ratio reported by Chin et al. (1996) yields a CS total column density of $N_{\text{CS}} = 2.9 \pm 1.1 \times 10^{17} \text{ cm}^{-2}$ with a peak optical depth of $\tau_{\text{CS}} = 32 \pm 12$, and therefore strongly optically thick. For completeness, we modelled the CS emission with the parameters above, together with a foreground component under $T=50 \text{ K}$ that absorbs both the background line and continuum emission. We note the good agreement between the velocity fit of CS, C^{33}S , and CH_3OCHO of $-2.46 \pm 0.15 \text{ km s}^{-1}$, $-2.3 \pm 0.16 \text{ km s}^{-1}$, and $2.0 \pm 0.3 \text{ km s}^{-1}$, with the absorption layer slightly blueshifted to $-3.4 \pm 0.2 \text{ km s}^{-1}$. The errors are obtained from the model fit to the lines.

We detect polarized emission from the CS ($J = 5 \rightarrow 4$) molecular line toward NGC6334I(N). The bottom-left panel of Figure 4 shows the polarized intensity spectrum and Figure 5 shows the channel maps. In the channel maps, we display the polarized CS emission as orange pseudo-vectors superposed on a coarsely plotted magnetic field morphology as inferred from polarized dust emission (shown as blue pseudo-vectors). Note, we are not applying a 90° rotation to the CS pseudo-vectors as we do to the polarized dust emission. The channel maps reveal good agreement between the hourglass magnetic-field morphology seen in the dust and the polarized CS emission observed as a function of velocity. For a more quantitative comparison between the field morphology and the polarized CS emission, we compute histograms of the differences in polarization position angles between the CS and the dust emission for different velocity channels (see Figure 6). The differences are calculated only at locations where the polarized CS emission overlaps with the polarized dust emission. Furthermore, we fit Gaussian profiles to histograms to derive probability density functions. All of the histograms are well centered around zero, within $\pm 10^\circ$ for the $\pm 4 \text{ km s}^{-1}$ range, with mostly symmetric Gaussian distributions suggesting that the CS polarized emission is correctly tracing the ‘‘hourglass’’ field morphology derived from dust (see Table 2 for the statistics). The best match is found at $V = -2 \text{ km s}^{-1}$ where $\langle \Delta\theta \rangle = 0^\circ$ and $\sigma_{\Delta\theta} = 6^\circ$ from the Gaussian fit. The V_{lsr} of NGC6334I(N) is about $\sim -3 \text{ km s}^{-1}$ and thus the best match is close to the systemic

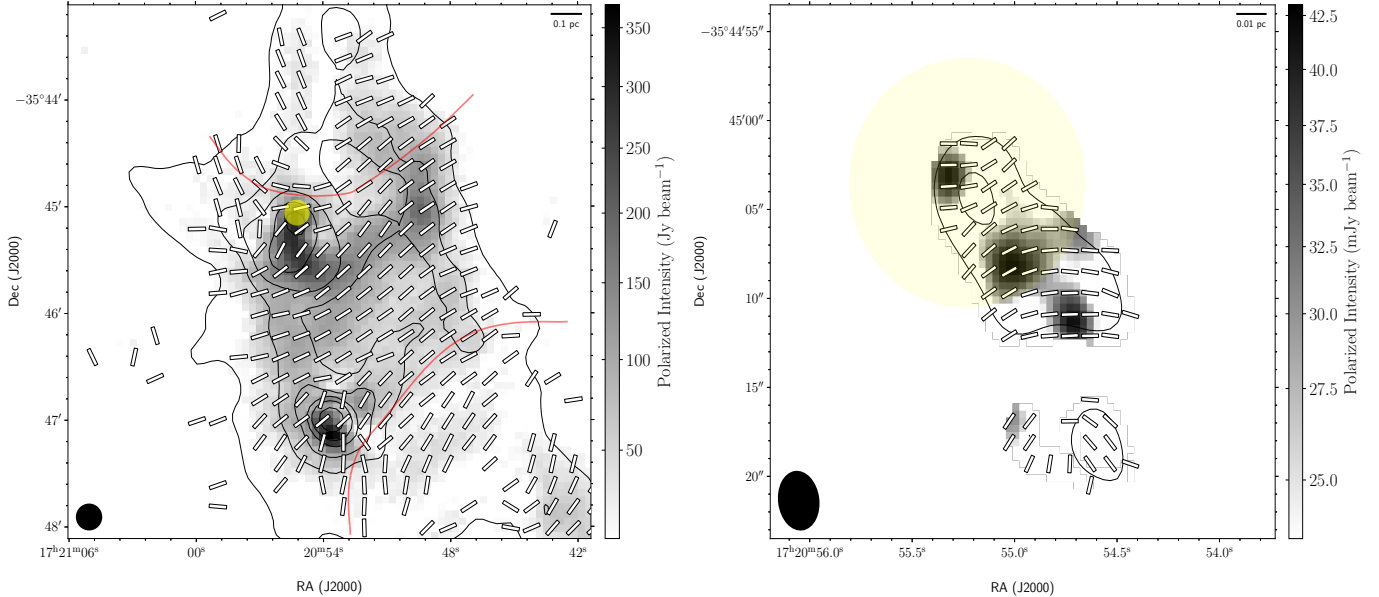


Figure 3. The magnetic field morphology onto the plane of the sky in NGC6334 as derived from polarized dust continuum emission data are shown here. *Left.* The map shows data obtained with the JCMT at $850 \mu\text{m}$ (Arzoumanian et al. 2021). The white line segments correspond to emission over $3\sigma = 6 \text{ mJy}$. The line segments are normalized and plotted, approximately, once per beam, where the beam size is $14''$; the beam is shown in the bottom-left corner as a solid, black circle. Gray scale shows the polarized intensity in Jy beam^{-1} , as indicated by the color bar. The contours correspond to the total intensity are plotted at levels of 0.51, 2.55, 5.1, 10.2, and $17.0 \text{ Jy beam}^{-1}$. The translucent red lines outlines the proposed “hourglass” pinched morphology for the magnetic field onto the plane of the sky. *Right.* Same as the left panel, but for SMA at $875 \mu\text{m}$ (Zhang et al. 2014). The white line segments correspond to emission debiased over 3σ , with $\sigma \sim 8 \text{ mJy beam}^{-1}$. The contours corresponds to step of 0.5 and 3 Jy beam^{-1} and gray-scale bar indicates the polarized flux in mJy beam^{-1} . The SMA beam is $2.''1 \times 2.''07$ at a positional angle of 20° . The yellow circle shows the ALMA region of interest in both maps.

Table 1. Statistics from Stokes Maps

Tracer	Velocity	I_p^a	σ_I^b	Q_p	σ_Q	U_p	σ_U	V_p	σ_V
	(km s^{-1})	(mJy beam^{-1})							
Dust	-	307	0.5	6.1	0.05	2.7	0.04	-0.25	0.023
CS	-6.0	326	7	2.6	0.7	-5.0	0.6	3.3	0.7
CS	-4.0	136	5	10.0	0.6	-4.8	0.5	-2.1	0.6
CS	-2.0	168	7	4.7	0.7	-3.9	0.6	2.7	0.7

^a The p subscript indicates peak intensity and it applies to all of the Stokes parameters.

^b The σ rms was estimated by choosing a region devoid of emission where the rms was obtained using the CASA task *imstat*.

velocity of the source. Although there are deviations between the magnetic field and the CS position angles, these are observed at the line-wings of the line suggesting a departure from the “hourglass” where the emission from the outflow becomes dominant. The polarized CS emission also seems to trace the magnetic field morphology along the dust cavity: see channel maps $v = -10$ to -2 km s^{-1} , which also show the blueshifted

lobe of the CS outflow. We note that the CS outflow appears to be orthogonal to the symmetry axis of the “hourglass” magnetic field. We will explore this finding in upcoming work (Cortes et al. in prep.). Additionally, we present channel maps of polarized emission from $\text{C}^{33}\text{S}(J = 5 \rightarrow 4)$ in Figure 7. Although the number of independent detections of polarization in the C^{33}S maps is smaller than for CS, the agreement with the CS polar-

ization position angle appears consistent across velocity space.

The number of independent polarization detections in the CS channel maps is large enough that we can also estimate the field strength using the DCF technique in a number of those channels (between -6 to -2 km s^{-1} ; for an description of what can be considered to be a sufficient number of channels, see Appendix A in Cortes et al. 2019). Over this channel range, we obtain an average field strength estimate of ~ 2 mG (see Table 3 for the channel-by-channel estimates). Polarized emission from molecular lines has a 90° ambiguity with respect to the ambient magnetic field direction (Goldreich & Kylafis 1981). However, this does not affect the estimation method because $\delta\phi$ will not change if the data is rotated by 90° . We will address the relation between the CS polarization pattern and the magnetic field in section 4.1.1.

4. DISCUSSION

4.1. The origin of the polarized CS emission

Linearly polarized emission from molecular lines was first detected in CS emission by Glenn et al. (1997) towards the IRC +10216 evolved star. Since then, it has been detected towards a number of sources, particularly in high-mass star forming regions (Girart et al. 1999; Lai et al. 2003; Cortes et al. 2005; Beuther et al. 2010; Hirota et al. 2020), and toward evolved stars (Vlemmings et al. 2012; Girart et al. 2013). Linearly polarized emission from molecular lines is expected when the magnetic sub-levels are unevenly populated because of anisotropies in the medium. Initial models assumed that large velocity gradients resulting from the kinematics were the dominant source of anisotropy (Goldreich & Kylafis 1982; Deguchi & Watson 1984). However, anisotropies in the radiation field can also affect the level populations and may be due to a geometrical distribution of the gas that produces optical depths that are not the same in all directions, or from embedded sources such as a protostellar core (in the case of star-forming regions; Cortes et al. 2005) or a star (in the case of a circumstellar shell around evolved sources; Vlemmings et al. 2012). Although it is expected that the amount of polarized emission will decrease with increasing optical depth as a result of photon trapping, we nevertheless find significant amounts of polarized emission across the CS spectrum in NGC6334I(N) (between 2% and $\sim 10\%$ within -20 to 20 km s^{-1} , see the bottom-left panel of Figure 4), for which our calculations show to be optically thick. Deguchi & Watson (1984) performed multi-level calculations for the CS ($J = 1 \rightarrow 0$) and ($J = 2 \rightarrow 1$) transitions and found linearly polarized emission at a level of $\sim 1\%$ for $\tau \sim 10$

with a significant decrease in fractional polarization for increasing τ . However, this computation is only one-dimensional and represents the best-case scenario where the optical depth is taken along the velocity gradient (see Figure 3 in Deguchi & Watson 1984). Cortes et al. (2005) also performed multilevel radiative transfer calculations for both CO ($J = 1 \rightarrow 0$) and ($J = 2 \rightarrow 1$) transitions, but this time adding a blackbody to the computation in order to introduce anisotropies in the radiation field. They found increasing amount of polarization as the line becomes optically thin (see Figure 7 in Cortes et al. 2005). Recently, Lankhaar & Vlemmings (2020) presented a comprehensive quantum mechanical treatment of the alignment of the molecule’s angular momentum by assuming only an anisotropic radiation field. Their treatment is fully three-dimensional, allowing for simulations of both radiative transfer and gas dynamics. Although they did not model CS emission in particular, their simple example of a collapsing spherical cloud produced polarization fractions for HCO^+ ($J = 3 \rightarrow 2$) and ($J = 2 \rightarrow 1$) at levels over 1% for radial distances beyond 600 au (~ 3 mpc) for the ($J = 3 \rightarrow 2$) and 900 au (~ 4.5 mpc) for the ($J = 2 \rightarrow 1$) transition. However, all of these calculations find that polarized line emission significantly decreases with higher optical depths. A possible explanation to this may be related to interferometric filtering and missing flux. Fractional polarization with interferometers has to be analyzed with care because of spatial filtering effects (Le Gouellec et al. 2020). The maximum recoverable angular scale for the configuration used to acquire these data is $\sim 5''$, which suggests that a significant fraction of the extended total intensity CS emission seen from the single dish (McCutcheon et al. 2000) might be filtered-out by ALMA and thus the fractional polarization values presented here are overestimated. This is because linearly polarized emission tend to be more compact than the total intensity emission. Estimating how far we are from the true fractional polarization will require sampling larger angular scales in full polarization mode, which the ALMA compact array (ACA) can do.

We also see significant amounts of fractional polarization at higher velocities (polarization levels $\gtrsim 10\%$ at $v < -20$ and $v > 20$ km s^{-1}). It is likely that, in these velocity ranges where the CS emission is tracing the outflow, the CS emission might be optically thin and thus the values estimated might be closer to the “true” fractional polarization values. The large velocity gradient and the radiation field from the embedded protostars are, most likely, the sources of anisotropy necessary to produce the large polarization fractions that we see there (see Cortes et al. 2005, Figure 7 for a CO

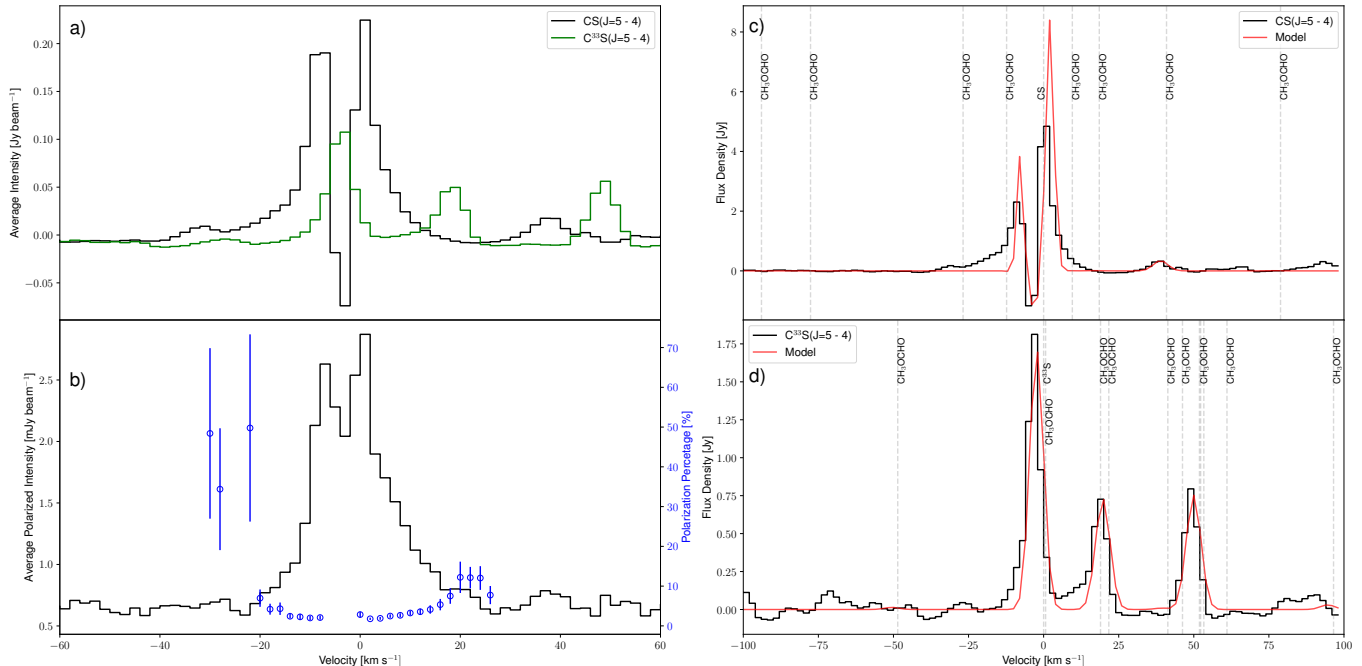


Figure 4. The CS spectra from the selected region in NGC6334I(N) is shown here (see Figure 2 for the region). **a)** The panel shows the total intensity and self-absorbed CS($J = 5 \rightarrow 4$) spectrum (blue) and the $C^{33}S(J = 5 \rightarrow 4)$ spectrum (green). **b)** The panel shows the CS debiased polarized intensity spectrum (black) with the fractional polarization of the CS emission superposed as circles with corresponding error bars. Note, we are not showing fractional polarization values for the range between -6 to -2 km s^{-1} because of the negative Stokes I due to self-absorption. **c)** The best fit to the CS, $C^{33}S$, and CH_3OCHO transitions is superposed on the observed CS spectra. In the figure, we are also indicating additional molecular line transitions that might be present given the spectral range. We clearly detect some complex organics such as methyl formate (CH_3OCHO). **d)** Same as (c) but for the $C^{33}S$ emission. The model was obtained by assuming LTE conditions, a $T_{\text{ex}} = 220$ K for $C^{33}S$, and a foreground screen of 50 K continuum to model the dust emission.

computation). We also note that strong polarization from CS is expected because of its large dipole moment ($\mu = 1.96$ D) compared with, for example, that of CO ($\mu = 0.12$ D), because of the μ^2 dependence of the radiative rates. Thus, it seems that the combination of anisotropies in both the radiation field and the gas kinematics is causing the strong CS polarized emission that we see in NGC6334I(N), where filtering effect might explain the large fractional polarization values seen when comparing to radiative transfer calculations. Nonetheless, 3-dimensional modeling of polarized CS emission will be needed to further understand the emission detected here, which is beyond the scope of this work.

Finally, if a foreground screen of molecular gas is present between the source and the telescope, some amount of linear polarization might be converted into circular polarization through anisotropic resonant scattering, or ARS (Houde et al. 2013b). The ARS will systematically corrupt the linear polarization position angle from the CS emission and change its relation respect to the ambient magnetic field. The ARS will manifest itself by the presence of statistical significant signal in Stokes V, which we do not detect. The peak emission is Stokes

V is about between -2.1 and 3.3 mJy beam^{-1} with a fractional level between 0.6 to 1.0% which is below the statistical uncertainty of $\sim 2\%$ that ALMA can measure (Cortes et al. 2021). The morphology of the Stokes V velocity channel maps are consistent with noise where the peaks alternate between positive and negative between channels which is inconsistent with a coherent conversion of linear to circular polarization by ARS (see Table 1 and Figure 9 in Appendix A for the Stokes V channel maps). Thus, we conclude that polarized emission from CS is purely linear and its relation to the field is subject to the known 90° ambiguity (see next section for a discussion).

4.1.1. The 90° ambiguity in the position angle of the polarized CS emission

Linearly polarized emission from molecular lines has a 90° ambiguity in the orientation of the polarization position angle with respect to the ambient magnetic field direction (Goldreich & Kylafis 1981). Thus, deriving the magnetic field morphology from the polarized CS emission has an additional degree of complexity versus the more straightforward method of deriving the field mor-

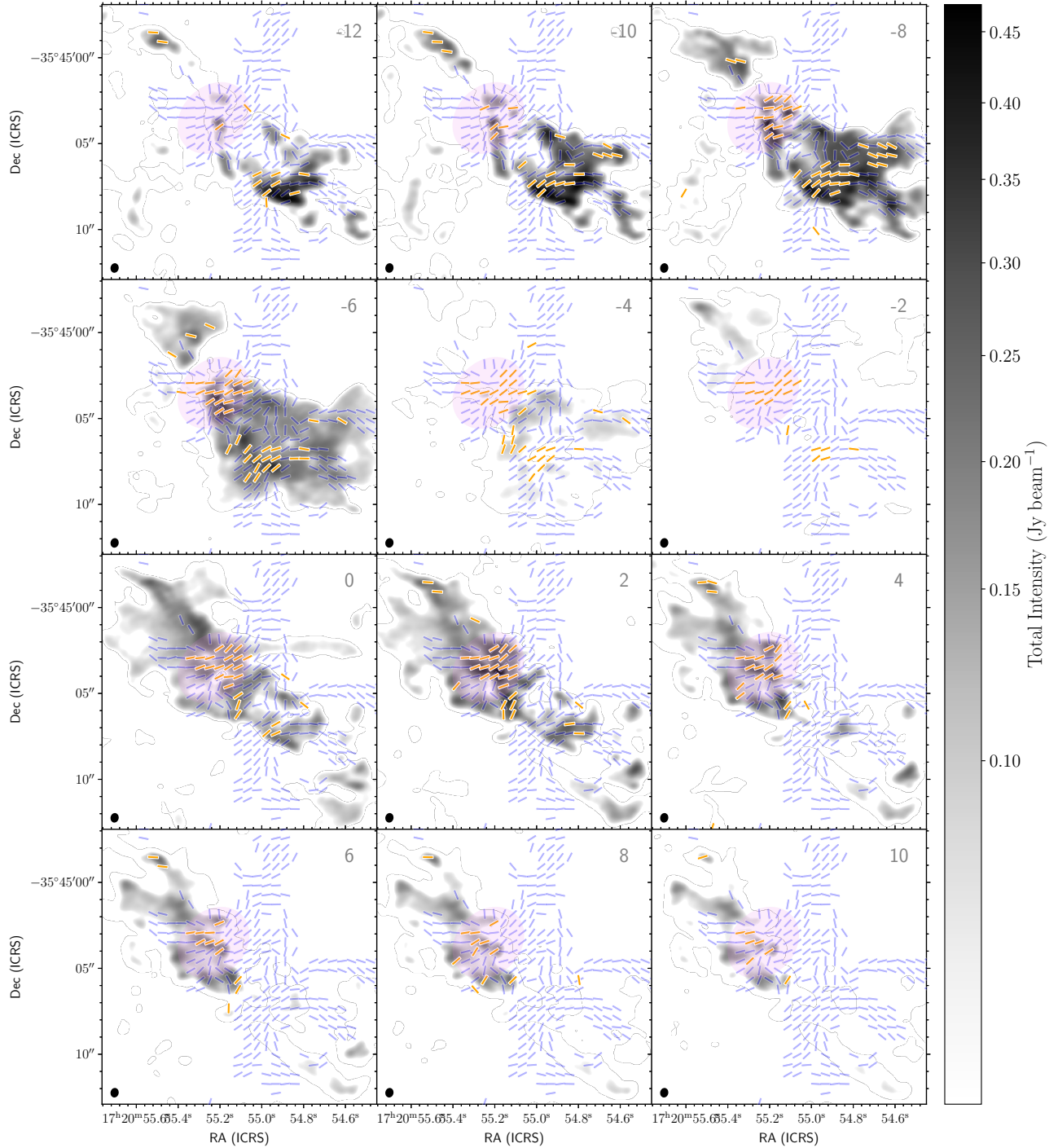


Figure 5. Velocity channel maps of the CS($J = 5 \rightarrow 4$) emission from NGC6334I(N) in the -12 to 10 km s^{-1} range. The velocity is indicated in km s^{-1} in the upper-right corner of each panel. We show the Stokes I CS emission in gray scale, the inferred magnetic field from polarized dust emission as blue pseudo-vectors, and the larger than 3σ significance CS polarization angles as orange pseudo-vectors, with $\langle \sigma \rangle = 780 \mu\text{Jy beam}^{-1}$ is the mean rms polarized intensity emission noise when considering all channels in the range. Note, the blue pseudo-vectors corresponding to the polarized dust emission show the inferred magnetic field morphology, having been rotated by 90° relative to the polarization. However, the polarization position angles from the polarized CS emission have not been rotated.

Table 2. Polarization Angle Statistics

Velocity	$\langle\Delta\phi\rangle^a$	$\text{std}(\Delta\phi)^b$	$\Delta\phi_0^c$	$\sigma_{\Delta\phi}^d$
(km s ⁻¹)	(°)	(°)	(°)	(°)
-12.0	8	25.9	21	-11.5
-10.0	9	20.1	16	17.4
-8.0	10	18.0	11	-17.4
-6.0	4	13.8	4	-13.1
-4.0	2	9.0	1	-8.4
-2.0	1	7.5	0	6.4
0.0	3	12.3	2	11.5
2.0	0	14.4	-2	7.6
4.0	-2	14.8	-5	-10.1
6.0	-2	15.6	-5	-7.4
8.0	-8	19.0	-6	6.2
10.0	-8	17.4	-8	6.9
12.0	-2	13.5	-4	8.7
14.0	-2	12.2	-7	8.0

^a Here $\langle\Delta\phi\rangle$ represents the mean of the difference values between dust and CS polarization angles.

^b Here $\text{std}(\Delta\phi)$ corresponds to the standard deviation of the difference values between the dust and the CS polarization angles.

^c Here $\Delta\phi_0$ corresponds to the center of a Gaussian fit to the distribution of polarization angle differences.

^d Here $\sigma_{\Delta\phi}$ corresponds to the width of a Gaussian fit to the distribution of polarization angle differences.

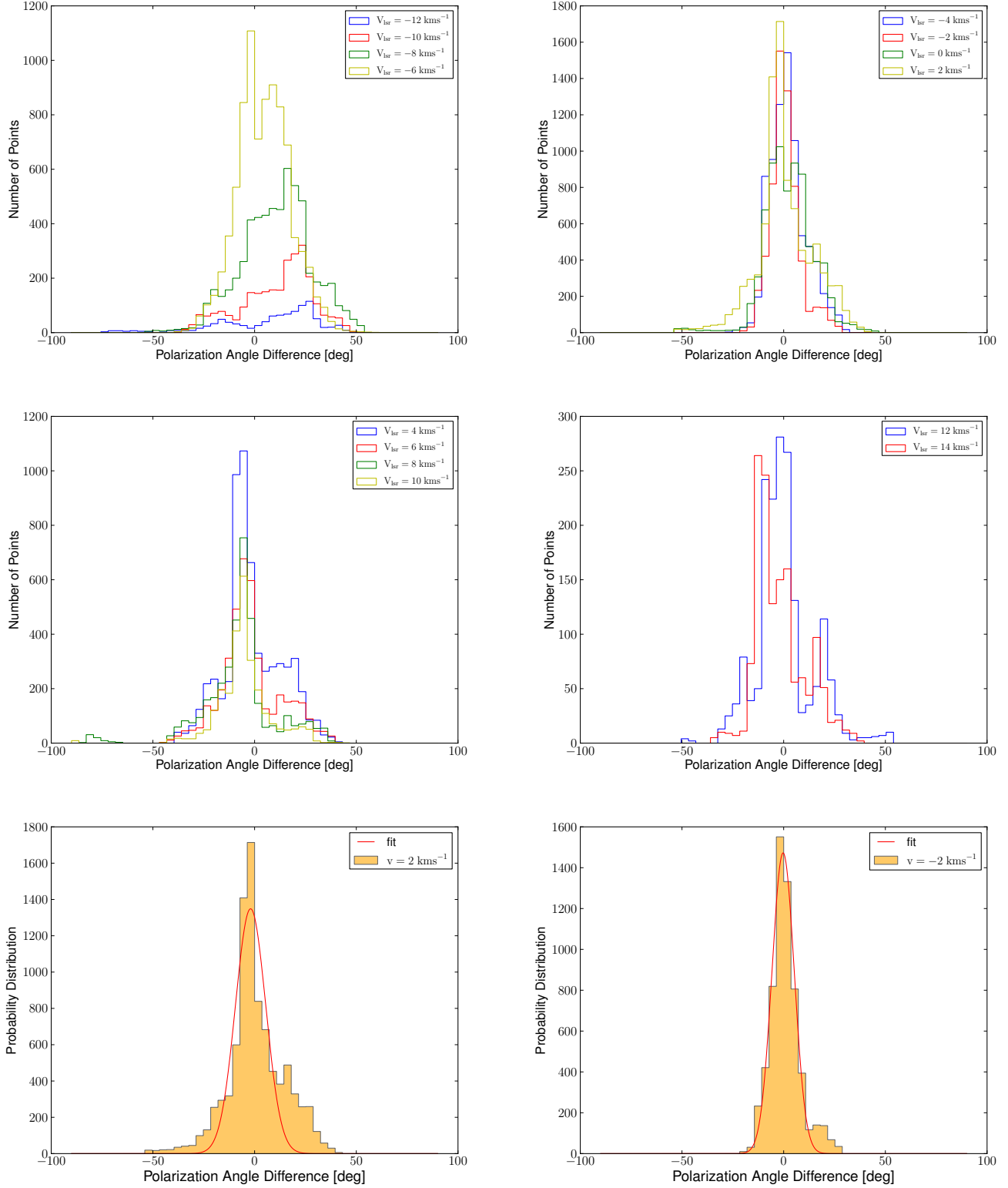


Figure 6. Histograms of differences in the polarization position angles of the dust and CS emission. We compute the differences inside the region used to estimate the field strength (see the purple ellipse in Figure 2). The panels are ordered as a function of velocity (from upper-left to lower-right), as indicated in legend in each plot. The best agreement is found at -2 and 2 km s^{-1} where Gaussian fits to the normalized histograms are shown in the two bottom panels. The fit parameters are listed in Table 6.

phology from polarized dust emission. To interpret the relationship between the CS polarization angle and the orientation of the ambient magnetic field, we use the inferred field morphology from the dust emission and arguments about physical plausibility. We interpret the position angle from the polarized CS emission as being parallel to the magnetic field onto the plane of the sky because of the close agreement between the hourglass magnetic field morphology seen in the dust and the polarization pattern of the CS emission, as shown in Figure 6 and Table 2. The opposite case, i.e., where the CS polarization is perpendicular to the inferred magnetic field from the dust, would imply an unrealistically complex field morphology over the central region of NGC6334I(N): because of the close agreement between CS and dust, the twisting of the field lines would have to be perpendicular at almost all positions and velocities shown in the channel maps. Such a situation is unheard of and likely nonphysical, even under strong rotation, which we do not have evidence for at the scales traced by the CS polarized emission. Our interpretation that the CS polarization traces the inferred magnetic field shape is also supported by the $C^{33}S(J = 5 \rightarrow 4)$ results, which agree well with the CS polarization, particularly at velocities of -4 and -2 km s^{-1} . These three independent polarization tracers show essentially the same result, which is a magnetic field morphology with an “hourglass” shape over the main cores in NGC6334I(N).

4.2. Tomography of magnetic fields

Hourglass magnetic field morphologies have long been predicted by magnetically regulated star formation models (e.g., Mouschovias 1976; Mouschovias & Morton 1985), and may be the result of ambipolar diffusion (Mouschovias 1991). This field morphology has been seen in a number of low- and high-mass star forming regions and at different length and mass scales (Schleuning 1998; Girart et al. 2006, 2009; Maury et al. 2018; Beltrán et al. 2019). In the magnetically regulated star formation scenario, a molecular cloud will initially be supported against gravitational collapse by the magnetic field, which is initially thought to be uniform. Because the neutrals are only weakly coupled to the charge carriers, which are held in place by the field, they will slowly diffuse past the magnetic field via ambipolar-diffusion. Because the field is frozen into the charge carriers, the field will be pinched attaining the hourglass shape. Alternatively, a self-gravitating core can also pull the field at the core center which will create an “hourglass” shape, but in this case ambipolar-diffusion might be a by-product of the process.

Although the “hourglass” shape seen in NGC6334I(N) is clear, the exquisite sensitivity and resolution of the ALMA data allow us to see local deviations from which the “hourglass” is a simple model. The density regime traced by ALMA is likely showing the result of complex physics which is difficult to explain without detailed numerical modeling, outside the scope of this paper. Furthermore, a clear “hourglass” field morphology in NGC6334I(N) is not seen at all length-scales. From the envelope scales traced by ALMA, to the core scales imaged by the SMA, and to the clump scales traced by the JCMT, the hourglass appears to be the shape of the magnetic field when we also consider NGC6334I (see Figures 2 and 3). However, at the cloud scales traced by Planck (see Figure 5 in Arzoumanian et al. 2021), the field is only pinched at the North-East side of the cloud. Whether this is a projection effect or not is not clear from the Figure alone where a detailed analysis of the Planck data would be required. Even though we cannot state with certainty that we see an “hourglass” field morphology as the ubiquitous shape across all length scales in NGC6334, the pinching in the field seen from cloud to the envelope scales is quite remarkable suggesting that the magnetic field is strong in this region. Furthermore, the field pattern seems also preserved in velocity space from -10 to 4 km s^{-1} at the ALMA scales, which is a 14 km s^{-1} range, almost three times the 5.3 km s^{-1} full width at half maximum (FWHM) line-width of $C^{33}S$ (our proxy for the turbulent motions).

Besides tracing a pinched field shape through multiple orders of magnitude in spatial scales, we are also tracing the field at different densities as well (from 10 to 10^7 cm^{-3} when considering density estimates from Li et al. 2015; Arzoumanian et al. 2021). The critical density for the CS ($J = 5 \rightarrow 4$) transition is $9 \times 10^6 \text{ cm}^{-3}$, which is obtained by assuming that the emission is optically thin. Because of the high optical depth estimated for the CS ($J = 5 \rightarrow 4$) transition, that number density is most likely smaller as the line may be sub-thermally excited. Shirley (2015) accounted for optical depth effects by computing the critical density considering photon trapping. Thus, the number density can be approximated to $n_{crit}^{thick} = n_{crit}^{thin} / \tau_{\nu_{jk}}$ when the optical depth is much larger than one, where n_{crit}^{thin} is the optically thin critical density and $\tau_{\nu_{jk}}$ is the line optical depth. From this assumption we obtain $n_{CS,crit}^{thick} = 2.8 \times 10^5 \text{ cm}^{-3}$. Note, here the $n_{CS,crit}^{thick}$ refers to the collisional partners involve in the excitation of the CS molecule which corresponds to H_2 . Although an abuse of notation, we use CS in the subscript to indicate that the density is derived from the CS emission. Furthermore, Shirley (2015) tabulated effective excitation densities for the CS molecule

by considering a number of rotational transitions. The effective excitation density is an empirical quantity defined by considering a 1 K km s^{-1} integrated emission. This quantity also takes into account optical depth effects such as radiation trapping (for a review, see [Evans 1999](#)). For the CS ($J = 5 \rightarrow 4$) transition, [Shirley \(2015\)](#) obtains $n_{\text{eff}} = 7.6 \times 10^4 \text{ cm}^{-3}$, assuming a kinetic temperature of 50 K, the dust temperature which is a good estimation of the kinetic temperature in the region of interest (see purple oval in Figures 2 and 5). Although these two estimates of the number density are close in value, detailed numerical radiative transfer modeling is required to obtain more accurate population numbers which we leave for future work. Nonetheless, the two criteria are reasonable approximations to the number density of the molecular hydrogen CS collisional partners under high optical depth conditions and thus we use the average as the estimate of the “true” number density, or $n_{\text{CS}} \sim 2 \times 10^5 \text{ cm}^{-3}$.

A value of $n_{\text{CS}} = 2 \times 10^5 \text{ cm}^{-3}$ is ~ 2 orders of magnitude less than the volume density estimated from the dust emission, which we calculated to be $4.2 \times 10^7 \text{ cm}^{-3}$. Thus, the polarized CS emission appears to be tracing the field at lower densities than the dust and at a level comparable with the JCMT observations. Therefore, within a single ALMA data-set we are not only tracing the “hourglass” shape as function of velocity, but also as a function of density: i.e., we are effectively performing magnetic field tomography. When we consider the evolution of the field morphology along these three axes (length-scale, velocity, and density), the striking coherence seen in the field structure strongly suggests that the magnetic field remains dynamically important from the diffuse to the high-density regime in NGC6334I(N).

4.3. *The dispersion function analysis and the strength of the magnetic field*

The DCF method does not consider the effects of finite angular resolution or integration along the line of sight, which at lower resolutions smooth out the polarized emission, reducing its dispersion, and therefore it might overestimate the field strength. Moreover, the effect of self-gravity in bending the field lines, which will affect the dispersion in the polarization position angle, is also not considered by DCF and its variants. Thus and because of the exquisite uv-coverage, resolution, and sensitivity of ALMA, local deviations in the position angle from the main field model, due to gravity, makes the applicability of the DCF method more challenging to the data. Here, we discuss how the different DCF variants used in this work attempt to correct the polarization position angle dispersion. To account for poor resolu-

tion in polarization maps, [Heitsch et al. \(2001\)](#) used the geometric mean between two modified DCF equations. The first modification attempts to address the small angle approximation by replacing the polarization angle dispersion by the dispersion of the tangent values of the position angle. The second modification attempts to deal with the case where the dispersion in the field lines is larger than the mean field. They do this by considering the 3-dimensional expansion of the field where all of the random components are assumed to be the same. This yields an equation also dependent on the dispersion of the tangent of the position angle values (see equation 11 [Heitsch et al. 2001](#)). Although consistent with their own simulations, their variant appears to underestimate the field strength when compared to other numerical results ([Falceta-Gonçalves et al. 2008](#)). In our data, this method yielded an estimate which is a factor ~ 10 smaller than the other estimates. It is likely that this is because local deviations from the “hourglass” main field morphology produced larger values when using the tangent function, which yields a larger dispersion and therefore a smaller estimate. In contrast, the modification proposed by [Falceta-Gonçalves et al. \(2008\)](#) was implemented by assuming that $\delta B/B$ is a global relation and thus they modified DCF by taking the tangent of the dispersion angle instead of $\delta\phi$ (see equation 9 in [Falceta-Gonçalves et al. 2008](#)). This was proposed to address larger angle dispersions due to an increasing turbulent component in the field. However, this will rapidly decrease the field strength as the tangent function quickly diverges for $\delta\phi > 60^\circ$. Recently, the DCF method was revisited and another correction was proposed which considers the compressible modes from small amplitude MHD waves (magnetosonic), instead of purely Alfvén transverse waves ([Skalidis & Tassis 2021](#)). This method implements a substitution in the DCF equation in the form of $\delta\phi \rightarrow \sqrt{\delta\phi}$, which seem to improve the recovery of the field strength when applied to their numerical simulations. Although it is not clear if the dominant mode perturbing the main field component is transverse (Alfvénic) or compressible (small amplitude magnetosonic waves), this variant will yield estimates which are smaller in value than the original DCF. The three previously described DCF variants used simulations to test the proposed modifications. All of the simulations assumed ideal MHD, which might not be representative of the physical conditions in NGC6334I(N). In fact, ideal MHD may produce artificially tangled magnetic field morphologies which will affect the polarization position angle dispersion, particularly in the line of sight. Furthermore and because of the low ionization rates in dense molecular clumps ($\sim 10^{-7}$),

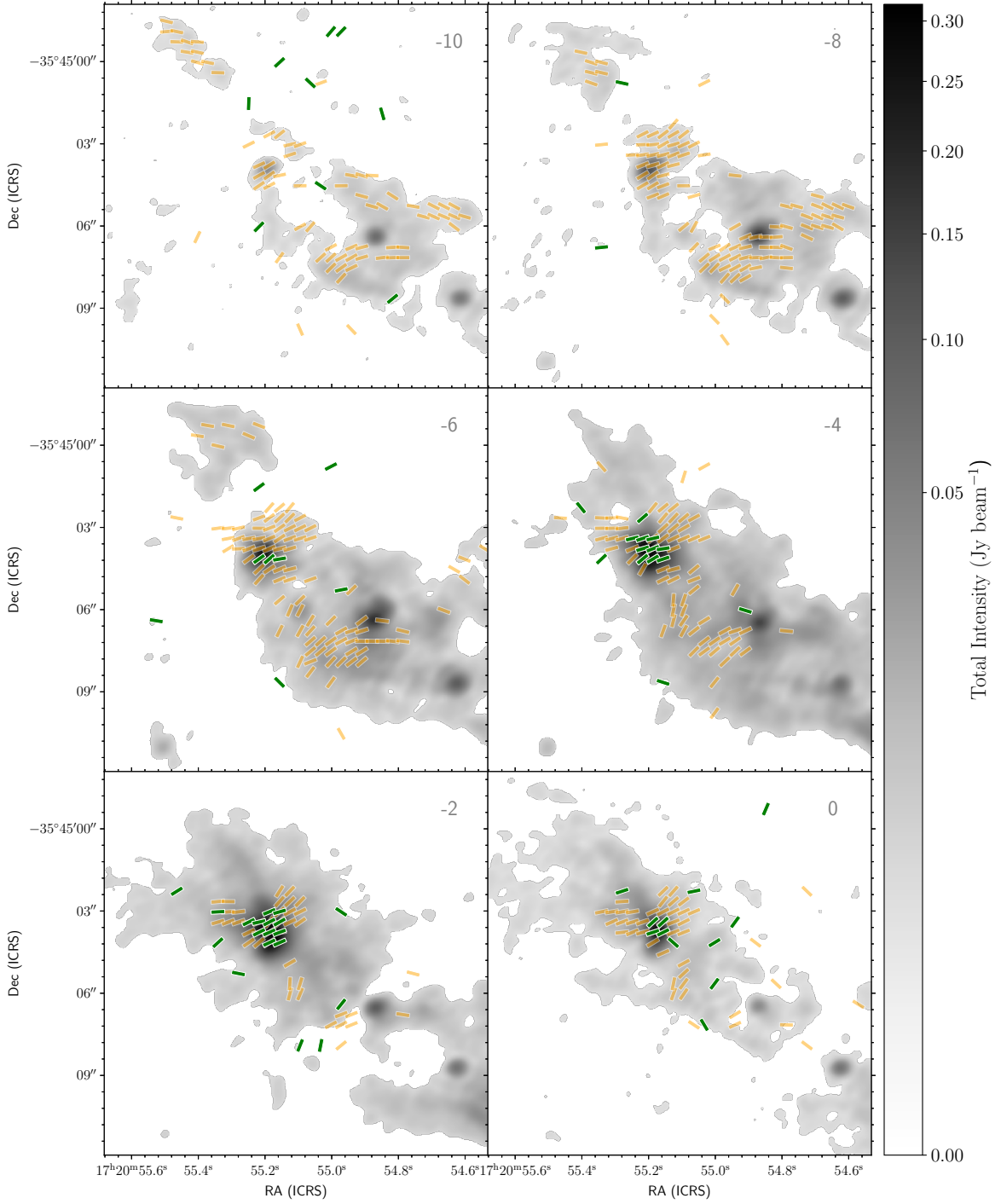


Figure 7. Same as Figure 5, but here we show the $C^{33}S(J = 5 \rightarrow 4)$ emission. The total intensity $C^{33}S$ emission is shown as a gray-scale. The polarized emission from CS is shown in orange pseudo-vectors while the polarized emission from $C^{33}S$ is shown in semi-transparent green pseudo-vectors. The significance of the polarization pseudo-vectors is 3σ after debiasing where the average channel map noise level, before debiasing, is $\langle\sigma\rangle = 770\mu\text{Jybeam}^{-1}$.

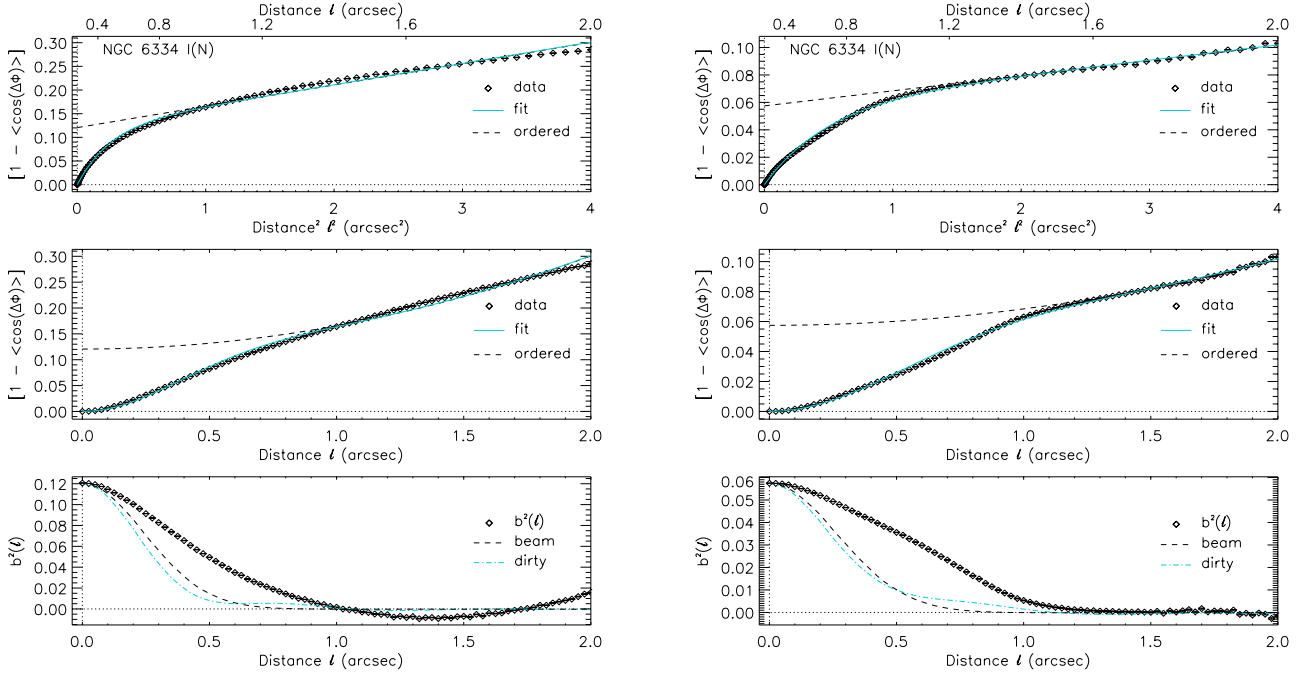


Figure 8. Dispersion analysis of the ALMA NGC6334I(N) data. **Left.** The dispersion function calculated as $[1 - \langle \cos(\Delta\phi) \rangle]$ (in symbols) is plotted as a function of l^2 at the top. The ordered component is also shown using a broken curve. The least-squares fit of the Gaussian turbulence model is plotted in turquoise as a solid curve. At the middle we also plot the dispersion function, but as a function of l . At the bottom, the signal-integrated turbulence autocorrelation function $b^2(l)$ (in symbols), along with the autocorrelated Gaussian beam (segmented curve), and the ALMA dirty beam (solid turquoise curve) are plotted. From the fit to the data, we derive turbulence correlation length of $\delta = 0''.262 \pm 0''.008$, or ~ 2 mpc, at the distance to NGC6334I(N), and $\langle B_t^2 \rangle / \langle B^2 \rangle = 0.29 \pm 0.01$. **Right.** Same as the left panel, but using the integrated CS polarized emission data over the velocity interval -6 to -2 km s^{-1} . The analysis yields a turbulence correlation length of $\delta = 0''.42 \pm 0''.011$, or ~ 2.6 mpc, and $\langle B_t^2 \rangle / \langle B^2 \rangle = 0.08 \pm 0.0013$.

non-ideal MHD effects, such as ambipolar diffusion, are unavoidable (Hennebelle & Inutsuka 2019).

The ADF method provides a way to quantify the turbulent component in the field and to better estimate the value of $\delta\phi$. This is done by fitting a structure function of the polarization position angle data, by incorporating a turbulence model, and also by considering the effects of interferometric filtering (for a summary of the technique see Section 2 of Houde et al. 2016). This analysis allow us to associate $\delta\phi = [\langle B_t^2 \rangle / \langle B^2 \rangle]^{1/2}$, where the quantity on the right-hand side is the ratio of turbulent to total magnetic energy, one of the quantities derived from the dispersion-function analysis. We can then use $\delta\phi$ to estimate the field strength in the plane of the sky via the usual DCF technique, which takes the form of

$$B_{\text{pos}} \simeq \sqrt{4\pi\rho\sigma(v)} \left[\frac{\langle B_t^2 \rangle}{\langle B^2 \rangle} \right]^{-1/2}, \quad (1)$$

where $\sigma(v) = \Delta V/2\sqrt{2\log 2}$, ΔV is the FWHM line-width of the C³³S line, and ρ is the volume density. By applying this analysis to the polarized dust emission data, considering the same region as before (see purple ellipse in Figure 2), we obtain a turbulence correlation length of $\delta = 0''.262 \pm 0''.008$, or ~ 2 mpc, at the distance to NGC6334I(N), and $\langle B_t^2 \rangle / \langle B^2 \rangle = 0.23 \pm 0.01$, which we use to estimate a plane-of-sky magnetic field strength $B_{\text{pos}} = 24$ mG (see Figure 8 and Table 3 for the results). Furthermore, we apply the same analysis to the CS polarized emission data considering a wide velocity range, and obtain a good fit between -6 to -2 km s⁻¹. In this interval, we find a turbulence correlation length of $\delta = 0''.42 \pm 0''.011$, or ~ 2.6 mpc, and $\langle B_t^2 \rangle / \langle B^2 \rangle = 0.08 \pm 0.0013$, which yields a plane-of-sky magnetic field strength $B_{\text{pos}} = 2.8$ mG. Note, the analysis was applied to the integrated data between -6 to -2 km s⁻¹, but given the small differences in $\delta\phi$ within the interval, we used the same $\langle B_t^2 \rangle / \langle B^2 \rangle$ value to estimate B_{pos} at each velocity channel (see Table 3). The differences in the field strength estimation is largely due to the differences in density used. That is, the dispersion analyses only contribute a factor of ~ 1.7 (lowering the dust estimate) while the densities increase the dust value by ~ 14 .

Recent work by Liu et al. (2021) analyzed ideal MHD simulations of proto-cluster formation at clump scales. They applied various statistical methods to synthetic magnetic field maps to study the applicability of the DCF method and the variants used here (including ADF). Because the magnetic morphology in NGC6334I(N) has an “hourglass” shape, it is likely that we are in the strong-field regime. Thus, Liu et al. results

suggests that the magnetic field strength estimates derived here are good to a factor of a few, again, subjected to the caveat of ideal MHD simulations.

We have five estimates for the field strength onto the plane of the sky. Each of them originate from modifications to the DCF method that try to address finite resolutions, the polarization angle dispersion value due to a random component of the field, and the effect of a different perturbation mode. Because none of these methods used here consider all of the relevant physics in this region, e.g. self-gravity, the “true” value for the field strength remains unconstrained. We lack an actual measurement of the field strength such the one provided by the Zeeman effect. Although still contested (see Jiang et al. 2020), results from Zeeman measurements show that the field strength will grow with density as a power law, or $\sim n^{2/3}$ (Crutcher & Kemball 2019). Thus, the DCF and its variants still give us a first order statistical approximation to the “true” magnetic field strength onto the plane of the sky. We quantify a final estimate by taking the average of all five estimates obtaining $\langle B_{\text{pos}} \rangle = 16$ mG as the average magnetic field onto the plane of the sky at densities of $n = 4.2 \times 10^7$ cm⁻³, and $\langle B_{\text{pos}} \rangle = 2$ mG at densities of $n = 2.0 \times 10^5$ cm⁻³ when considering the polarized CS emission.

4.4. Comparison with other HMSFR

By comparing our results from NGC6334I(N) to other HMSFR, we seek to discover if there is a pattern in the physical conditions of regions where the magnetic field has a clear and distinctive shape, such as an “hourglass” morphology. Examples of similar magnetic field morphologies to NGC6334I(N) are cores like G240 where the “hourglass” magnetic field, appears as a “textbook” case for magnetic controlled star formation with a bipolar outflow closely aligned to both the rotation and magnetic field axes (Qiu et al. 2014). Note, the G240 mass, 95 M_⊙, is substantially larger than the ~ 26 M_⊙ of the combined 1b and 1c core masses in NGC6334I(N) as derived from our data inside the purple oval region shown in Figure 2. Another example is the massive core G31.41, with a mass comparable to NGC6334I(N) (about 26 M_⊙ from Beltrán et al. 2019), has also been shown to exhibit an “hourglass” magnetic field morphology from core (Girart et al. 2009) to envelope scales (Beltrán et al. 2019). However, the alignment between the outflow, rotation, and magnetic axes is less clear here when compared to G240. The length-scales where the “hourglass” shape is traced in these two sources are similar to what we see in NGC6334I(N). For instance, in G31.41 the field morphology is seen preserved through a scale range that matches the lower

end in the NGC6334I(N) scales. The data obtained from G240 traces the field at the core scales also where the “hourglass” is seen in NGC6334I(N). However, not all HMSFRs show “hourglass” magnetic field morphologies. For instance, in the W43-Main molecular complex, the W43-MM1 (Cortes et al. 2016; Arce-Tord et al. 2020) and W43-MM2 clumps (Cortes et al. 2019) exhibit magnetic field morphologies that are primarily radial over their most massive cores, which is expected when gravity dominates the dynamics. W43-Main harbors some of the most massive protostars currently known ($\gtrsim 100 M_{\odot}$, Cortes et al. 2016; Motte et al. 2018; Cortes et al. 2019), whereas the mass of the central cores in NGC6334I(N) are only about $\sim 26 M_{\odot}$ in total when considering our data. However and because of the angular scales sampled by our ALMA data, we might be missing flux which might make NGC6334I(N) appear less massive than other regions. Nonetheless, this difference in core mass is not significant when comparing W43-Main with G240 where the core masses are comparable, but the field shapes are completely different. A totally different magnetic field morphology is seen in IRAS 180089-1732 where the field was found to have an spiral morphology (Sanhueza et al. 2021). Previous mapping of this source at clump scales appears to show the same field pattern (Beuther et al. 2010) as seen by ALMA at envelope scales. In this case, the total core mass is estimated to be $75 M_{\odot}$ from the ALMA data, which is also comparable to G240 and in the lower range from the W43-Main estimates. Thus, it is also uncertain whether the core mass is a decisive factor to explain the differences in the field shape seen across these HMSFRs.

High mass star forming cores are usually surrounded by H II regions which provide significant radiative feedback. It is possible that radiation pressure coming from H II regions may compress the field in conjunction with the effects of gravity, which the field may resist if strong enough (e.g. see Li et al. 2006; Shariff et al. 2019, for an example in the Carina nebula). For instance, W43-Main is part of a giant molecular complex which has at its center a large H II region powered by a number of O7 Wolf-Rayet stars, which appear to be not only ionizing the boundaries of W43-Main but also compressing the gas (Blum et al. 1999; Motte et al. 2003), while NGC6334 contains a group of smaller H II regions known as the “Cat’s Paw” which seem distributed along the filament (Russeil et al. 2016). This also seems to be the case for G31.41, which is surrounded by both compact and extended H II regions (J. M. Girart private communication). In contrast, for G240 and IRAS 180089-1732, the situation seems unclear as the cores appear to be more isolated than NGC6334I(N), G31.41, and

W43-Main. Although we note these differences, in this simple analysis we are certainly ignoring a number of other factors such as chemical diversity, stage of evolution, possible initial conditions, among many others. Thus, acquiring sufficient statistical cases is paramount to increase our understanding about how stars form in high mass star forming regions and what is the role of the magnetic field. As part of this MagMaR project, we have acquired a comprehensive sample that is sufficiently large to allow us to begin addressing these questions in future work.

5. SUMMARY AND CONCLUSIONS

We present ALMA observations of polarized dust, CS($J = 5 \rightarrow 4$), and C³³S($J = 5 \rightarrow 4$) emission towards NGC6334I(N). From these data we find:

- The magnetic field derived from the ALMA polarized dust emission data shows a clear “hourglass” morphology over the 1b, 1c, and possibly 1a cores. This shape is preserved from clump to envelope scales when considering both the SMA and JCMT data.
- We obtained polarized emission from CS and C³³S $J = 5 \rightarrow 4$ transition. We modelled the total intensity for both the CS and C³³S lines using the MADCUBA software; we calculate optical depths of 32 and 0.1 for each line, respectively.
- The polarized emission from CS nicely traces the same magnetic field “hourglass” morphology inferred from the polarized dust emission within the -12 to 10 km s⁻¹ velocity range. We estimated a number density of 2×10^5 cm⁻³ as traced by the CS emission; 2 order of magnitude less than the 4.2×10^7 cm⁻³ derived from dust emission. This allow us to obtain a tomographic view of the field in this region from a single dataset.
- We also report polarized emission from C³³S. While there are fewer independent detections of polarization, the polarized emission appears consistent with the CS results.
- We estimate the magnetic field strength onto the plane of the sky from both the dust and the CS data by using multiple methods. We obtain an average field strength estimate of $\langle B_{\text{pos}} \rangle = 16$ mG from the dust and $\langle B_{\text{pos}} \rangle \sim 2$ mG from the CS emission, when considering the -6 to -2 km s⁻¹ velocity range.

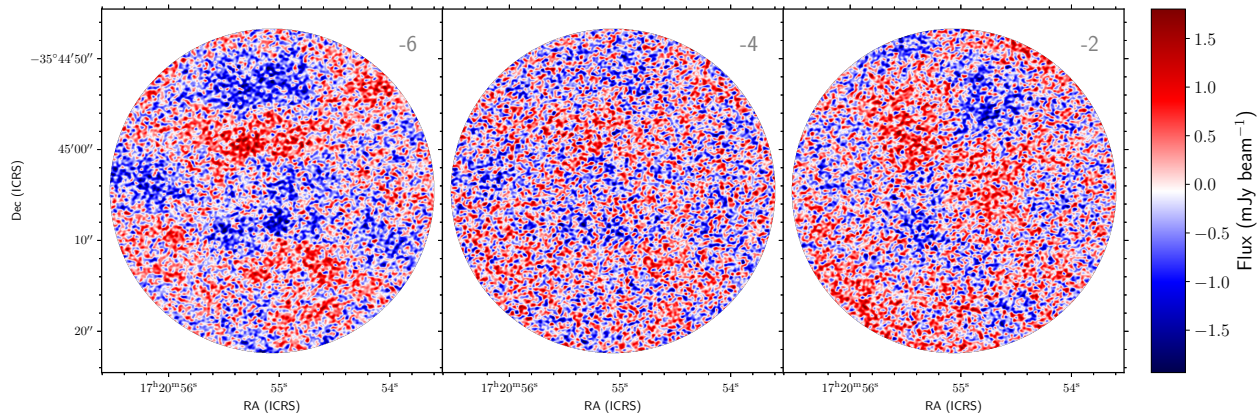


Figure 9. The velocity channel maps for the flat, not primary beam corrected, Stokes V are shown here from -6 to -2 km s^{-1} using a divergent color scheme to indicate both negative and positive values. The velocity of each channel is indicated in the top right corner at each map.

APPENDIX

A. STOKES V VELOCITY CHANNEL MAPS

Figure 9 shows the Stokes V velocity channel maps for the range between -6 to -2 km s^{-1} which we used to estimate the magnetic field strength onto the plane of the sky. The maps statistics are given in Table 1. Although there seem to be some structure in the maps, this structure is not consistent with the compact linear polarization that we see from CS and what we would expect if ARS were happening in NGC6334I(N). This structure is likely off-axis instrumental leakage which is under the current ALMA accuracy (Hull et al. 2020; Cortes et al. 2021). Additionally, we show the integrated CS emission map superposed to the polarized dust emission; note, not the inferred magnetic field onto the plane of the sky (see Figure 10). We are showing the unbiased data to show the full extent of the data. The integrated CS emission map was averaged in uv-space over the range of the line and both polarization pattern appear to be orthogonal to each other as expected based on the argumentation exposed in this work (see section 4).

B. THE NORMALIZATION PROBLEM

It was recently discovered that strong molecular line emission can be detected in the auto-correlations of ALMA data, thereby biasing the spectrally-resolved normalization, and sometimes the nominally off-source T_{sys} calibration measurements detect unrelated astronomical line emission. This problem will affect the calibrated fluxes obtained from molecular line emission biasing the determination of any astrophysical quantity derived from such fluxes. A re-normalization strategy was put in place by ALMA which corrects for this effect including the polarization data reported here (Moellenbrock 2021). We detect the CS($J = 5 \rightarrow 4$) line only in the auto-correlations and not in the T_{sys} spectra. By applying the aforementioned ALMA correction, we estimate that the error introduced in $\sigma_\phi < 0.5^\circ$ for the polarization position angle and $\sigma_{P_{\text{frac}}} = 0.01\%$, which are essentially negligible for the scope of this work. Although we find small errors in these quantities, we do find noticeable differences in the Stokes spectra. The difference is because the polarization position angle and the fractional polarization are derived from ratios of the Stokes parameter which cancel out the normalization effect. Therefore, data that requires modeling of the Stokes parameters (e.g. Zeeman measurements), should carefully apply this correction and inspect the spectra appropriately.

Facilities: ALMA.

Software: APLpy, an open-source plotting package for Python hosted at <http://aplpy.github.com> (Robitaille &

Bressert 2012). CASA (McMullin et al. 2007). Astropy (Astropy Collaboration et al. 2018). MADCUBA (Martín et al. 2019).

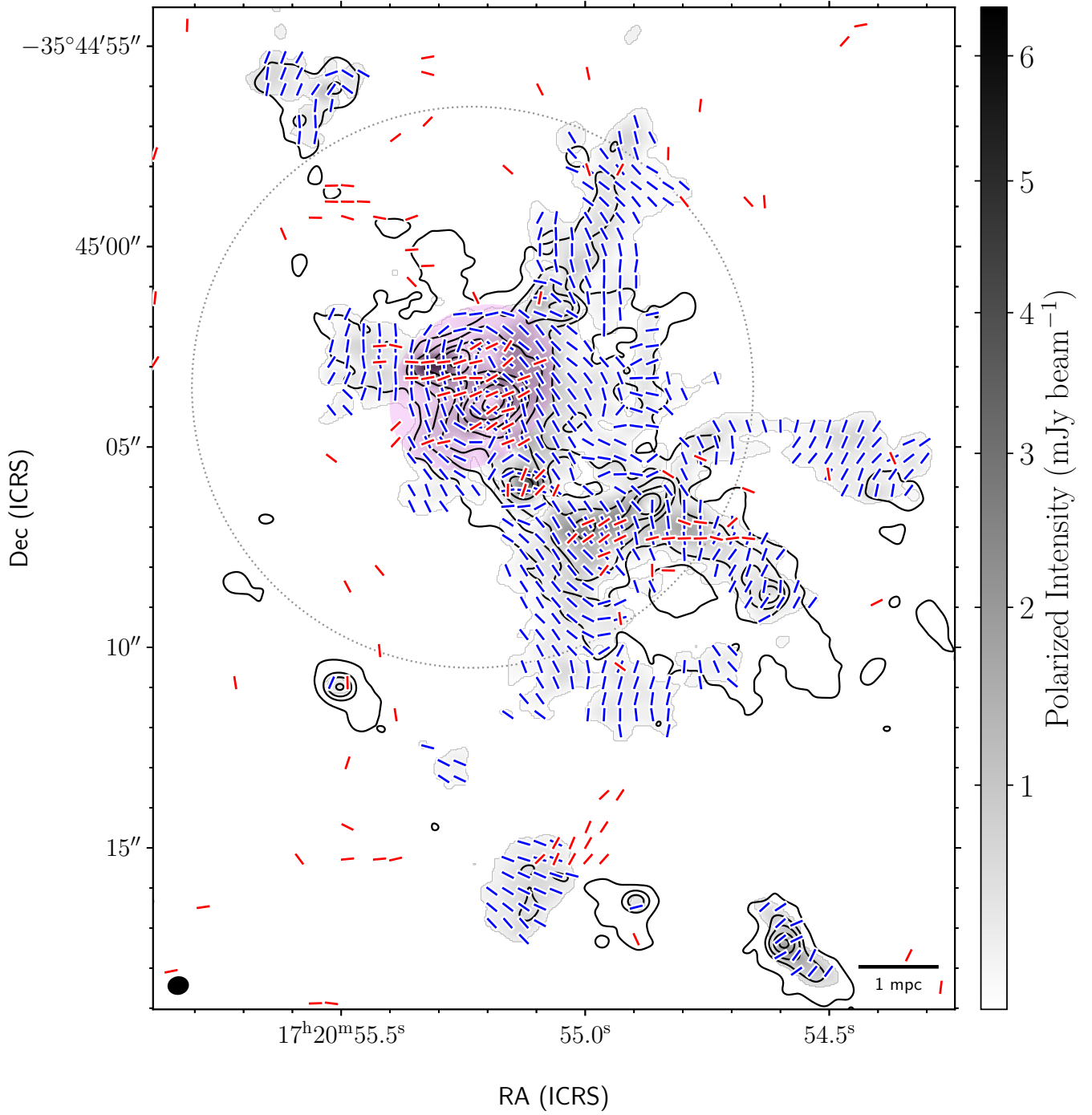


Figure 10. Here we show un-biased polarization maps from both dust (blue) and CS (red) emission. The Figure follows the same layout at Figure 2. The CS polarization maps was produced by imaging a continuum subtracted, u-v averaged, measurement sets. The first session was uv-averaged between 244.919 to 244.968 GHz while the second session was uv-averaged between 244.935 to 244.984 GHz.

Table 3. Magnetic Field Strength Estimations

Tracer	Velocity	N^a	n	$\langle\phi\rangle^b$	$\delta\phi^b$	ΔV	B_1^c	B_2^d	B_3^e	B_4^f	B_5^g	$\langle B_t \rangle^2 / \langle B \rangle^2$
	[km s^{-1}]	[10^{24} cm^{-2}]	[10^5 cm^{-3}]	[$^\circ$]	[$^\circ$]	[km s^{-1}]	[mG]	[mG]	[mG]	[mG]	[mG]	
Dust	-	2.0	423.9	29.3	29.4	5.3	21.9	19.9	1.4	23.6	11.1	0.23 ± 0.01
CS	-6.0	2.0	2.0	179.3	6.7	5.3	3.24	3.18	0.060	2.75	1.58	0.08 ± 0.001
CS	-4.0	2.0	2.0	179.2	6.5	5.3	2.49	2.40	0.116	2.75	1.39	0.08 ± 0.001
CS	-2.0	2.0	2.0	179.3	6.2	5.3	2.39	2.31	0.165	2.75	1.36	0.08 ± 0.001

^a The column density corresponds to the region used to extract $\delta\phi$.

^b $\langle\phi\rangle$ is the average polarization position angle (PA) and $\delta\phi$ is the PA dispersion (calculated using circular statistics).

^c Estimations of the magnetic field, in the plane of the sky, done with the original DCF method.

^d Estimations of the magnetic field in the plane of the sky, done using the corrections implemented by Equation 9 in [Falceta-Gonçalves et al. \(2008\)](#).

^e Estimations of the magnetic field in the plane of the sky, done using the corrections implemented by Equation 12 in [Heitsch et al. \(2001\)](#).

^f Magnetic field strength estimated by using the ratio of turbulent to total magnetic energy.

^g Magnetic field strength estimated by using the DCF modification proposed by [Skalidis & Tassis \(2021\)](#).

ACKNOWLEDGMENTS

P.C.C. would like to thank A. Sanchez-Monge and M. Sadaghiani for providing machine readable tables from their data. P.C.C. acknowledges publication support from ALMA and NRAO. P.S. was partially supported by a Grant-in-Aid for Scientific Research (KAKENHI Number 18H01259) of the Japan Society for the Promotion of Science (JSPS). M.H.'s research is funded through the Natural Sciences and Engineering Research Council of Canada Discovery Grant RGPIN-2016-04460. C.L.H.H. acknowledges the support of the NAOJ Fellowship and JSPS KAKENHI grant 20K14527. C.L.H.H. and J.M.G. acknowledge the support of JSPS KAKENHI grant 18K13586. J.M.G. acknowledges the support of the Spanish grant AYA2017-84390-C2-R (AEI/FEDER, UE). L.A.Z acknowledges financial support from CONACyT-280775 and UNAM-PAPIITIN110618 grants, Mexico. This paper makes use of the following ALMA data: 2018.1.00105.S. ALMA is a partnership of ESO (representing its member states), NSF (USA) and NINS (Japan), together with NRC (Canada), MOST and ASIAA (Taiwan), and KASI (Republic of Korea), in cooperation with the Republic of Chile. The Joint ALMA Observatory is operated by ESO, AUI/NRAO and NAOJ. The National Radio Astronomy Observatory is a facility of the National Science Foundation operated under cooperative agreement by Associated Universities, Inc.

REFERENCES

- André, P., Revéret, V., Könyves, V., et al. 2016, *A&A*, 592, A54, doi: [10.1051/0004-6361/201628378](https://doi.org/10.1051/0004-6361/201628378)
- Arce-Tord, C., Louvet, F., Cortes, P. C., et al. 2020, *A&A*, 640, A111, doi: [10.1051/0004-6361/202038024](https://doi.org/10.1051/0004-6361/202038024)
- Arzoumanian, D., Furuya, R. S., Hasegawa, T., et al. 2021, *A&A*, 647, A78, doi: [10.1051/0004-6361/202038624](https://doi.org/10.1051/0004-6361/202038624)
- Astropy Collaboration, Price-Whelan, A. M., Sipőcz, B. M., et al. 2018, *AJ*, 156, 123, doi: [10.3847/1538-3881/aabc4f](https://doi.org/10.3847/1538-3881/aabc4f)
- Beltrán, M. T., Padovani, M., Girart, J. M., et al. 2019, *A&A*, 630, A54, doi: [10.1051/0004-6361/201935701](https://doi.org/10.1051/0004-6361/201935701)
- Beuther, H., Vlemmings, W. H. T., Rao, R., & van der Tak, F. F. S. 2010, *ApJL*, 724, L113, doi: [10.1088/2041-8205/724/1/L113](https://doi.org/10.1088/2041-8205/724/1/L113)
- Blum, R. D., Damineli, A., & Conti, P. S. 1999, *AJ*, 117, 1392, doi: [10.1086/300791](https://doi.org/10.1086/300791)
- Bonnell, I. A., Larson, R. B., & Zinnecker, H. 2007, in *Protostars and Planets V*, ed. B. Reipurth, D. Jewitt, & K. Keil, 149–164
- Bonnell, I. A., Vine, S. G., & Bate, M. R. 2004, *MNRAS*, 349, 735, doi: [10.1111/j.1365-2966.2004.07543.x](https://doi.org/10.1111/j.1365-2966.2004.07543.x)
- Chandrasekhar, S., & Fermi, E. 1953, *ApJ*, 118, 113
- Chibueze, J. O., Omodaka, T., Handa, T., et al. 2014, *ApJ*, 784, 114, doi: [10.1088/0004-637X/784/2/114](https://doi.org/10.1088/0004-637X/784/2/114)
- Chin, Y. N., Henkel, C., Whiteoak, J. B., Langer, N., & Churchwell, E. B. 1996, *A&A*, 305, 960. <https://arxiv.org/abs/astro-ph/9505067>
- Cortes, P., Remijan, A., Biggs, A., et al. 2021, *ALMA Cycle 8 2021 Technical Handbook*, doi: [10.5281/zenodo.4612218](https://doi.org/10.5281/zenodo.4612218)
- Cortes, P. C., Crutcher, R. M., & Watson, W. D. 2005, *ApJ*, 628, 780, doi: [10.1086/430815](https://doi.org/10.1086/430815)
- Cortes, P. C., Girart, J. M., Hull, C. L. H., et al. 2016, *ApJL*, 825, L15, doi: [10.3847/2041-8205/825/1/L15](https://doi.org/10.3847/2041-8205/825/1/L15)
- Cortes, P. C., Hull, C. L. H., Girart, J. M., et al. 2019, *ApJ*, 884, 48, doi: [10.3847/1538-4357/ab378d](https://doi.org/10.3847/1538-4357/ab378d)
- Crutcher, R. M., & Kemball, A. J. 2019, *Frontiers in Astronomy and Space Sciences*, 6, 66, doi: [10.3389/fspas.2019.00066](https://doi.org/10.3389/fspas.2019.00066)

- Davis, L. 1951, *Phys. Rev.*, 81, 890,
doi: [10.1103/PhysRev.81.890.2](https://doi.org/10.1103/PhysRev.81.890.2)
- Deguchi, S., & Watson, W. D. 1984, *ApJ*, 285, 126,
doi: [10.1086/162483](https://doi.org/10.1086/162483)
- Evans, II, N. J. 1999, *ARA&A*, 37, 311,
doi: [10.1146/annurev.astro.37.1.311](https://doi.org/10.1146/annurev.astro.37.1.311)
- Falceta-Gonçalves, D., Lazarian, A., & Kowal, G. 2008,
ApJ, 679, 537, doi: [10.1086/587479](https://doi.org/10.1086/587479)
- Fernández-López, M., Sanhueza, P., Zapata, L. A., et al.
2021, arXiv e-prints, arXiv:2104.03331.
<https://arxiv.org/abs/2104.03331>
- Girart, J. M., Beltrán, M. T., Zhang, Q., Rao, R., &
Estalella, R. 2009, *Science*, 324, 1408,
doi: [10.1126/science.1171807](https://doi.org/10.1126/science.1171807)
- Girart, J. M., Crutcher, R. M., & Rao, R. 1999, *ApJL*, 525,
L109
- Girart, J. M., Frau, P., Zhang, Q., et al. 2013, *ApJ*, 772, 69,
doi: [10.1088/0004-637X/772/1/69](https://doi.org/10.1088/0004-637X/772/1/69)
- Girart, J. M., Rao, R., & Marrone, D. P. 2006, *Science*,
313, 812, doi: [10.1126/science.1129093](https://doi.org/10.1126/science.1129093)
- Glenn, J., Walker, C. K., Biegging, J. H., & Jewell, P. R.
1997, *ApJL*, 487, L89, doi: [10.1086/310863](https://doi.org/10.1086/310863)
- Goldreich, P., & Kylafis, N. D. 1981, *ApJL*, 243, L75
— 1982, *ApJ*, 253, 606
- Heitsch, F., Zweibel, E. G., Mac Low, M.-M., Li, P., &
Norman, M. L. 2001, *ApJ*, 561, 800, doi: [10.1086/323489](https://doi.org/10.1086/323489)
- Hennebelle, P., & Inutsuka, S.-i. 2019, *Frontiers in
Astronomy and Space Sciences*, 6, 5,
doi: [10.3389/fspas.2019.00005](https://doi.org/10.3389/fspas.2019.00005)
- Hildebrand, R. H. 1983, *QJRAS*, 24, 267
- Hildebrand, R. H., Kirby, L., Dotson, J. L., Houde, M., &
Vaillancourt, J. E. 2009, *ApJ*, 696, 567,
doi: [10.1088/0004-637X/696/1/567](https://doi.org/10.1088/0004-637X/696/1/567)
- Hirota, T., Plambeck, R. L., Wright, M. C. H., et al. 2020,
ApJ, 896, 157, doi: [10.3847/1538-4357/ab959e](https://doi.org/10.3847/1538-4357/ab959e)
- Houde, M., Fletcher, A., Beck, R., et al. 2013a, *ApJ*, 766,
49, doi: [10.1088/0004-637X/766/1/49](https://doi.org/10.1088/0004-637X/766/1/49)
- Houde, M., Hezareh, T., Jones, S., & Rajabi, F. 2013b,
ApJ, 764, 24, doi: [10.1088/0004-637X/764/1/24](https://doi.org/10.1088/0004-637X/764/1/24)
- Houde, M., Hull, C. L. H., Plambeck, R. L., Vaillancourt,
J. E., & Hildebrand, R. H. 2016, *ApJ*, 820, 38,
doi: [10.3847/0004-637X/820/1/38](https://doi.org/10.3847/0004-637X/820/1/38)
- Houde, M., Vaillancourt, J. E., Hildebrand, R. H.,
Chitsazzadeh, S., & Kirby, L. 2009, *ApJ*, 706, 1504,
doi: [10.1088/0004-637X/706/2/1504](https://doi.org/10.1088/0004-637X/706/2/1504)
- Hull, C. L. H., Le Gouellec, V. J. M., Girart, J. M., Tobin,
J. J., & Bourke, T. L. 2019, arXiv e-prints,
arXiv:1910.07290. <https://arxiv.org/abs/1910.07290>
- Hull, C. L. H., & Plambeck, R. L. 2015, *Journal of
Astronomical Instrumentation*, 4, 1550005,
doi: [10.1142/S2251171715500051](https://doi.org/10.1142/S2251171715500051)
- Hull, C. L. H., & Zhang, Q. 2019, *Frontiers in Astronomy
and Space Sciences*, 6, 3, doi: [10.3389/fspas.2019.00003](https://doi.org/10.3389/fspas.2019.00003)
- Hull, C. L. H., Girart, J. M., Tychoniec, L., et al. 2017,
ApJ, 847, 92, doi: [10.3847/1538-4357/aa7fe9](https://doi.org/10.3847/1538-4357/aa7fe9)
- Hull, C. L. H., Cortes, P. C., Gouellec, V. J. M. L., et al.
2020, *PASP*, 132, 094501, doi: [10.1088/1538-3873/ab99cd](https://doi.org/10.1088/1538-3873/ab99cd)
- Hunter, T. R., Brogan, C. L., Cyganowski, C. J., & Young,
K. H. 2014, *ApJ*, 788, 187,
doi: [10.1088/0004-637X/788/2/187](https://doi.org/10.1088/0004-637X/788/2/187)
- Hunter, T. R., Brogan, C. L., MacLeod, G., et al. 2017,
ApJL, 837, L29, doi: [10.3847/2041-8213/aa5d0e](https://doi.org/10.3847/2041-8213/aa5d0e)
- Jiang, H., bai Li, H., & Fan, X. 2020, *The Astrophysical
Journal*, 890, 153, doi: [10.3847/1538-4357/ab672b](https://doi.org/10.3847/1538-4357/ab672b)
- Kirk, J. M., Ward-Thompson, D., Palmeirim, P., et al.
2013, *MNRAS*, 432, 1424, doi: [10.1093/mnras/stt561](https://doi.org/10.1093/mnras/stt561)
- Krumholz, M. R., Stone, J. M., & Gardiner, T. A. 2007,
ApJ, 671, 518, doi: [10.1086/522665](https://doi.org/10.1086/522665)
- Lai, S., Girart, J. M., & Crutcher, R. M. 2003, *ApJ*, 598,
392
- Lankhaar, B., & Vlemmings, W. 2020, *A&A*, 636, A14,
doi: [10.1051/0004-6361/202037509](https://doi.org/10.1051/0004-6361/202037509)
- Le Gouellec, V. J. M., Hull, C. L. H., Maury, A. J., et al.
2019, *ApJ*, 885, 106, doi: [10.3847/1538-4357/ab43c2](https://doi.org/10.3847/1538-4357/ab43c2)
- Le Gouellec, V. J. M., Maury, A. J., Guillet, V., et al. 2020,
A&A, 644, A11, doi: [10.1051/0004-6361/202038404](https://doi.org/10.1051/0004-6361/202038404)
- Li, H., Griffin, G. S., Krejny, M., et al. 2006, *ApJ*, 648, 340,
doi: [10.1086/505858](https://doi.org/10.1086/505858)
- Li, H.-B., Yuen, K. H., Otto, F., et al. 2015, *NatAs*, 520,
518, doi: [10.1038/nature14291](https://doi.org/10.1038/nature14291)
- Liu, J., Zhang, Q., Commercon, B., et al. 2021, arXiv
e-prints, arXiv:2106.09934.
<https://arxiv.org/abs/2106.09934>
- Martín, S., Martín-Pintado, J., Blanco-Sánchez, C., et al.
2019, *A&A*, 631, A159,
doi: [10.1051/0004-6361/201936144](https://doi.org/10.1051/0004-6361/201936144)
- Maury, A. J., Girart, J. M., Zhang, Q., et al. 2018,
MNRAS, 477, 2760, doi: [10.1093/mnras/sty574](https://doi.org/10.1093/mnras/sty574)
- McCutcheon, W. H., Sandell, G., Matthews, H. E., et al.
2000, *MNRAS*, 316, 152,
doi: [10.1046/j.1365-8711.2000.03487.x](https://doi.org/10.1046/j.1365-8711.2000.03487.x)
- McKee, C. F., & Tan, J. C. 2003, *ApJ*, 585, 850,
doi: [10.1086/346149](https://doi.org/10.1086/346149)
- McMullin, J. P., Waters, B., Schiebel, D., Young, W., &
Golap, K. 2007, in *Astronomical Society of the Pacific
Conference Series*, Vol. 376, *Astronomical Data Analysis
Software and Systems XVI*, ed. R. A. Shaw, F. Hill, &
D. J. Bell, 127

- Moellenbrock, G. 2021, In preparation
- Motte, F., Schilke, P., & Lis, D. C. 2003, *ApJ*, 582, 277
- Motte, F., Nony, T., Louvet, F., et al. 2018, *Nature Astronomy*, 2, 478, doi: [10.1038/s41550-018-0452-x](https://doi.org/10.1038/s41550-018-0452-x)
- Mouschovias, T. C. 1976, *ApJ*, 207, 141, doi: [10.1086/154478](https://doi.org/10.1086/154478)
- . 1991, *ApJ*, 373, 169, doi: [10.1086/170035](https://doi.org/10.1086/170035)
- Mouschovias, T. C., & Morton, S. A. 1985, *ApJ*, 298, 205, doi: [10.1086/163599](https://doi.org/10.1086/163599)
- Ossenkopf, V., & Henning, T. 1994, *A&A*, 291, 943
- Planck Collaboration XXXV, Ade, P. A. R., Aghanim, N., et al. 2016, *A&A*, 586, A138, doi: [10.1051/0004-6361/201525896](https://doi.org/10.1051/0004-6361/201525896)
- Qiu, K., Zhang, Q., Menten, K. M., et al. 2014, *ApJL*, 794, L18, doi: [10.1088/2041-8205/794/1/L18](https://doi.org/10.1088/2041-8205/794/1/L18)
- Robitaille, T., & Bressert, E. 2012, *APLpy: Astronomical Plotting Library in Python*. <http://ascl.net/1208.017>
- Russeil, D., Tigé, J., Adami, C., et al. 2016, *A&A*, 587, A135, doi: [10.1051/0004-6361/201424484](https://doi.org/10.1051/0004-6361/201424484)
- Sadaghiani, M., Sánchez-Monge, Á., Schilke, P., et al. 2020, *A&A*, 635, A2, doi: [10.1051/0004-6361/201935699](https://doi.org/10.1051/0004-6361/201935699)
- Sanhueza, P., Girart, J. M., Padovani, M., et al. 2021, *ApJL*, 915, L10, doi: [10.3847/2041-8213/ac081c](https://doi.org/10.3847/2041-8213/ac081c)
- Schleuning, D. A. 1998, *ApJ*, 493, 811
- Shariff, J. A., Ade, P. A. R., Angilè, F. E., et al. 2019, *The Astrophysical Journal*, 872, 197, doi: [10.3847/1538-4357/aaff5f](https://doi.org/10.3847/1538-4357/aaff5f)
- Shirley, Y. L. 2015, *PASP*, 127, 299, doi: [10.1086/680342](https://doi.org/10.1086/680342)
- Skalidis, R., & Tassis, K. 2021, *A&A*, 647, A186, doi: [10.1051/0004-6361/202039779](https://doi.org/10.1051/0004-6361/202039779)
- Sridharan, T. K., Rao, R., Qiu, K., et al. 2014, *ApJL*, 783, L31, doi: [10.1088/2041-8205/783/2/L31](https://doi.org/10.1088/2041-8205/783/2/L31)
- Vaillancourt, J. E. 2011, in *Astronomical Society of the Pacific Conference Series*, Vol. 449, *Astronomical Polarimetry 2008: Science from Small to Large Telescopes*, ed. P. Bastien, N. Manset, D. P. Clemens, & N. St-Louis, 169
- Vlemmings, W. H. T., Ramstedt, S., Rao, R., & Maercker, M. 2012, *A&A*, 540, L3, doi: [10.1051/0004-6361/201218897](https://doi.org/10.1051/0004-6361/201218897)
- Wardle, J. F. C., & Kronberg, P. P. 1974, *ApJ*, 194, 249, doi: [10.1086/153240](https://doi.org/10.1086/153240)
- Zhang, Q., Qiu, K., Girart, J. M., et al. 2014, *ApJ*, 792, 116, doi: [10.1088/0004-637X/792/2/116](https://doi.org/10.1088/0004-637X/792/2/116)